Variance Orientation Transform

Die Früherkennung der Osteoarthrose in dem trabekulären Gewebe des Knies

BACHELORARBEIT

zur Erlangung des akademischen Grades

Bachelor of Science

im Rahmen des Studiums

Medizinische Informatik

eingereicht von

Ștefan Ovidiu Oancea
Matrikelnummer 1227706

an der Fakultät für Informatik

der Technischen Universität Wien

Betreuung: Dipl.-Ing. Dr.techn. Eduard Gröller

Wien, 17. März 2016

Ștefan Ovidiu Oancea	Eduard Gröller

FAKULTÄT
FÜR !NFORMATIK
Faculty of Informatics

Variance Orientation Transform

Detection of Early Osteoarthritis in Knee Trabecular Bone

BACHELOR'S THESIS

submitted in partial fulfillment of the requirements for the degree of

Bachelor of Science

in

Medical Informatics

by

Ștefan Ovidiu Oancea
Registration Number 1227706

to the Faculty of Informatics
at the TU Wien
Advisor: Dipl.-Ing. Dr.techn. Eduard Gröller

Vienna, 17th March, 2016

Ștefan Ovidiu Oancea   Eduard Gröller

Erklärung zur Verfassung der Arbeit

Ștefan Ovidiu Oancea
Vienna

Hiermit erkläre ich, dass ich diese Arbeit selbständig verfasst habe, dass ich die verwendeten Quellen und Hilfsmittel vollständig angegeben habe und dass ich die Stellen der Arbeit – einschließlich Tabellen, Karten und Abbildungen –, die anderen Werken oder dem Internet im Wortlaut oder dem Sinn nach entnommen sind, auf jeden Fall unter Angabe der Quelle als Entlehnung kenntlich gemacht habe.

Wien, 17. März 2016

Ștefan Ovidiu Oancea

Danksagung

Erstens möchte ich mich bei meiner Familie für ihre bedingungslose Unterstützung während diesen akademischen Jahren bedanken. Sie waren die Quelle meiner Motivation wegzufahren um eine sehr gute Universität zu absolvieren.

Zweitens möchte ich mich bei allen meinen Professoren an der TU Wien für Ihren Enthusiasmus bedanken. Sie haben mich immer neugirieg behalten, Ihre Lehrveranstaltungen jedesmal zu besuchen.

Nicht zuletzt, möchte ich mich bei meinen Kollegen von Braincon Handels-GmbH (`http://braincon.com/`) ebenfalls bedanken. Die Materialen und Ressourcen, die sie zur Verfügung gestellt haben, machten diese Arbeit möglich.

Acknowledgements

Firstly, I would like to thank my family for their unconditional support throughout these academic years and for the motivation they have given me to leave home to finish a very good university.

Secondly, I would like to thank all the enthusiasthic professors at the Vienna University of Technology for making their subjects so interesting, that they convinced me to visit their courses with pleasure every time.

Last but not least, I would like to thank my colleagues at Braincon Handels-GmbH (`http://braincon.com/`) for providing materials and resources and thus making this work possible.

Kurzfassung

Seit die fraktalen Eigenschaften des trabekulären Knochens eines Knies entdeckt wurden, schenkt man den Methoden zur fraktalen Analyse einer 2D Knochenoberfläche mehr Beachtung. Das hat zum Teil damit zu tun, dass Röntgenaufnahmen die billigste bildgebende Technik im klinischen Routinescreening ist und zum anderen wurde gezeigt, dass trabekuläre Knochen des arthrotischen Patienten zu Deformierungen führen, lange bevor der charakteristische Gelenkschwund auftritt. Das ultimative Ziel eines solchen Algorithmus würde die Differenzierung von gesundem und ungesundem trabekulären Knochens sein.

Diese Arbeit präsentiert meinen Report über meine Implementierung des „Variance Orientation Transform“ (VOT) Algorithmus, eine fraktale Methode, welche anders als vergleichbare Methoden, die Möglichkeit bietet die Knochenstruktur in verschiedenen Richtungen und über verschiedene Maßstäbe zu quantifizieren. Es basiert auf der Idee, dass ein einzelner fraktaler Dimensionswert nicht genug für die Beschreibung einer solch komplexen Struktur wie der eines trabekulären Knochen ist. Aus diesem Grund berechnet VOT mehr deskriptive fraktale Dimensionen, was man auch als fraktale Signatur bezeichnet (engl. ‘fractal signatures’, kurz FSs)

Im Kapitel 1 und 2 wird der Leser in den Begriff der Fraktale und deren theoretischen Hintergründen sowie in den theoretischen Hintergründen des VOT Algorithmus eingeführt. Im Kapitel 3 werden ähnliche Techniken für die Analyse von trabekulären Knochen vorgestellt und im Kapitel 4 mein praktischer Versuch der Implementierung des VOT Algorithmus im Detail erläutert; zudem wird im selben Kapitel der VOT durch die Benützung von künstlich erzeugten fraktalen Oberflächen überprüft und seine Fähigkeit zwischen gesunden und ungesunden Knochen zu differenzieren wird untersucht. Das 5. und letzte Kapitel fasst weiter mögliche Ideen zur Verbesserung und Testung des Algorithmus zusammen.

Abstract

Since the fractal properties of the knee trabecular bone were discovered, fractal methods for analyzing bone surface radiographic projections have gained more attention. This is partly due to the fact that radiography is the cheapest imaging technique in routine clinical screening and partly due to the fact that it was shown that the trabecular bones of osteoarthritic patients indicate early deformations, even long before the characteristic join loss occurs. The ultimate goal of such an algorithm would be to differentiate healthy from unhealthy trabecular bone.

This paper presents a report of our implementation of the Variance Orientation Transform (VOT) algorithm, a fractal method, which unlike other similar methods, is able to quantify bone texture in different directions and over different scales of measurement. It is based on the idea that a single fractal dimension value is not enough to describe such a complex structure as the trabecular bone and thus, VOT calculates more descriptive fractal dimensions called fractal signatures (FSs).

In Chapters 1 and 2 we introduce the notion of fractals and the theoretical background behind them and the VOT algorithm. In Chapter 3 similar techniques for analyzing trabecular bone are presented and in Chapter 4 our particular attempt at implementing VOT is described in detail; moreover, in the same Chapter VOT is validated using some artificially generated fractal surfaces and the ability of differentiating healthy and affected bone is also investigated. The last Chapter, Chapter 5, covers further possible ideas of improving and testing of the algorithm.

Contents

CHAPTER 1

Introduction

The human bone can be formed out of two types of osseous tissue: the *cortical bone* (also known as the *compact bone*) and the *cancellous bone* (also known as the *trabecular bone*, in short, *TB* or *spongy bone* — Figure 1.1). The latter is of particular importance to the present work due to its special characteristics.

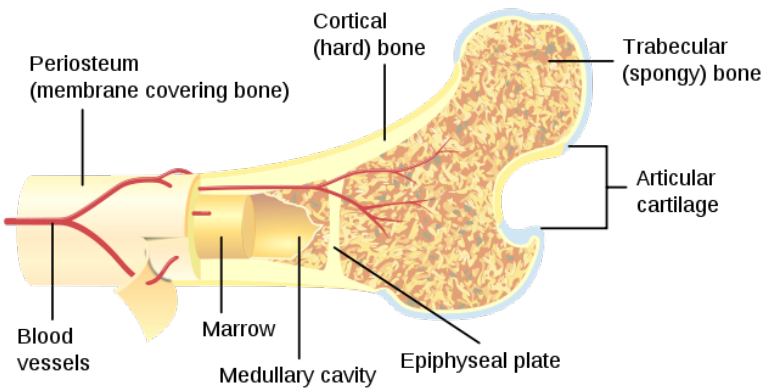

Figure 1.1: Cross-Section of a long bone showing the difference in structure between trabecular and cortical bones. Image courtesy of Wikipedia user Pbroks13, licensed under CC BY 3.0 (`http://creativecommons.org/licenses/by/3.0/`).

Usually a trabecular bone can be found at the end of long bones, such as for example the tibia. This tissue is significantly less dense than the cortical bone, rendering it less resistant to fracture and more prone to bone degeneration which happens for example during the onset of Osteoarthritis (OA). The particular structure of the trabecular tissue plays an important role in transferring mechanical load from joints along the bone (along the midshaft[1]). Due to its spatial arrangement, high stress concentrations are avoided, i.e., the stress is dissipated. This basically means that the greatest 'strength' of the bone is also its greatest weakness. The smallest functional unit within the cancellous bone is called *trabecula* (Figure 1.2) and it has recently been shown that the alignment of the trabecular network is strongly influenced by the mechanical load distribution within the bone [GMH+14].

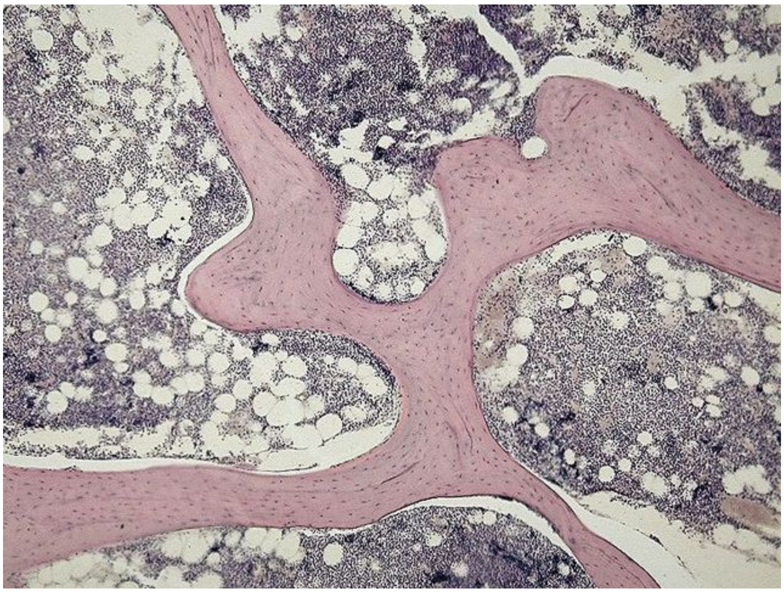

Figure 1.2: Cancellous bone under the microscope: the rose channels represent the *trabeculae*, while the dark blue stains represent the bone marrow. Image courtesy of Department of Histology, Jagiellonian University Medical College `http://www.histologia.cm-uj.krakow.pl/index.html`.

Already the early stages of OA produce rather significant changes in composition and organization of the TB. For example, not only the formation of abnormally thick and vertical trabeculae can be observed, but also an increase in BVF (bone volume fraction) [KWCZ95, KWCZ]. Usually, OA is strongly linked to articular cartilage loss. Most detection methods are therefore targeted in detecting cartilage degeneration while overlooking other possible early indications of OA, which were shown to settle long before the cartilage even begins to decay [BW04].

To address the matter stated above, Wolski developed some methods that are capable of assessing the TB roughness and integrity only based on X-ray images of the knee joint ([WPS09]). Among these methods there is also the most promising one called *Variance Orientation Transform*, or simply *VOT*, which is also the topic of this work.

[1] midway between the epiphyses of a long bone. Source: `http://medical-dictionary.thefreedictionary.com/`

Even though the method is a bit far from producing the wanted outcome, its results so far have shown that the idea is clearly on the right track. Wolski himself stated that once such a tissue-based decision-making system (that can tell the difference between an affected and a non-affected bone — the ultimate goal) will be mature, 'it could be used for clinical studies such as the evaluation of effects of medication, intra-articular injections, or surgical interventions on the progression of OA' [WPS09, p. 1].

This work focuses on implementing and last but not least, validating the VOT algorithm described by Wolski. This is done because the method is very promising and shows great room for improvements, which shall be introduced and further studied in our future works. The investigation of the VOT algorithm requires understanding of some properties that the TB (and its radiographic images) exhibits, properties that also make the theory behind it applicable in this particular case. Wolski lists these properties in [PSD$^+$10, p. 1]:

1. TB exhibits fractal properties, i.e., it is (visually) self-similar over a wide range of scales. Moreover, the TB hides self-similar processes in it. As Lopes and Betrouni put it [LB09, p. 635], 'the measured length increases as the scale of measurement increases. Thus, in fractal geometry, the Euclidean concept of "length" becomes a process rather than an event, and this process is controlled by a constant parameter'. The mentioned parameter is the so-called *Hurst coefficient*, a very important parameter in the study of self-similar processes in statistics;
2. Radiography is the cheapest and most popular imaging technique used in routine clinical screening;
3. The radiograph is a 2D projection containing data directly related to the underlying 3D TB structure;
4. TB texture images contain information that is useful for the prediction of knee OA.

Every notion that is still unclear up to this point, such as *fractal properties, self-similarity, scales, Hurst coefficient etc.*, will be explained in Chapter 2, which covers the entire theoretical background behind the VOT algorithm.

CHAPTER 2

Background

2.1 Fractals

In 1983 Benoît Mandelbrot introduced the notion of *fractal geometry* [Man83]. This type of geometry differs strongly from the 'traditional' *Euclidean geometry* by being able to analyze and quantify very complex shapes, signals or structures. In the same book mentioned above, Mandelbrot defines a *fractal* as following: *"a rough or fragmented geometric shape that can be split into parts, each of which is (at least approximately) a reduced-size copy of the whole"*. The term *fractal* has been first used by the author already in the year 1975 in need of characterizing a complex object that lacked integrity and order. His idea stemmed from the Latin word *fractus* which translates to *broken* or *fractured*.

A structure, a surface or a shape is thus considered being a *fractal* when it possesses a defining set of features, called *fractal properties*. These properties are put together by Falconer [Fal04, p. 13]. He says that when F is a fractal, the following properties will apply most of the cases:

P1. F has a fine structure, that is, detail on arbitrarily small scales.

P2. F is too irregular to be described in traditional geometrical language, both locally and globally.

P3. Often F has some form of self-similarity, perhaps approximate or statistical.

P4. Usually the *fractal dimension* of F (defined in some way) is greater than its *topological dimension*.

P5. In most cases of interest, F is defined in a very simple way, perhaps recursively.

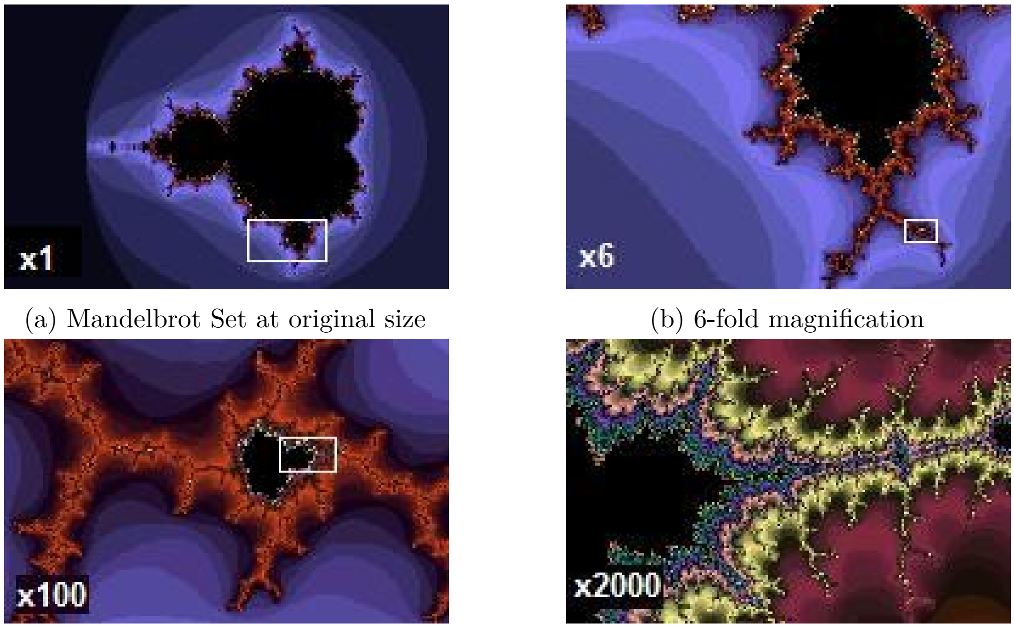

(a) Mandelbrot Set at original size

(b) 6-fold magnification

(c) 100-fold magnification

(d) 2000-fold magnification

Figure 2.1: Mandelbrot Set at different scales. Images licensed under GPL (General Public License).

Four out of five properties listed above are pretty self-explanatory and thus no further elaborations are made regarding them. Instead, the fractal example from Figure 2.1, which is also widely-known as the *Mandelbrot Set*, can very well illustrate those characteristics. Thus, in all four images, 2.1a, 2.1b, 2.1c and 2.1d, the fragmented state of the structure can be clearly seen (property *P2*). It is impossible to describe such structures by making use of just angles and lengths of segments, as it is usually done with Euclidean geometry. Further, properties *P1* and *P5* can be observed in 2.1d. There are infinitely, alike-looking, many elements that compose the structure. Last but not least, property number 3 can be understood when considering all four images in turn. It is obvious that there are some elements that keep reappearing when considering the structure at different scales.

A single property, namely property *P4*, was omitted in the visual analysis from the previous paragraph. The reason is that it is impossible to understand the meaning of it just by comparing or observing the images above. This property also contains two terms that are of particular significance in the field of fractal geometry and last but not least in the investigation of the VOT method: *fractal dimension* (also known as *Hausdorff–Besicovitch dimension*) and topological dimension. The meaning of the terms and of the property as a whole will be clarified in the following sections, as they play an important role in the present work.

2.2 Fractals in nature and humans

Usually, such fractal behavior, as described in Section 2.1, can often be observed in the complicated fabric of nature. The nature with its intricate patterns was actually the reason why Mandelbrot introduced a whole new way of analyzing these patterns with a hope of gaining a better understanding of the phenomenon.

A series of examples of how intricate the patterns of nature are can begin with the fern, an ancient, primitive plant (cf. Figure 2.2a). It can be easily observed that within the leaves of the fern the same branching pattern repeats itself over and over again, beginning with the stalk. Another example from the same class of so-called *branching fractals* is the basin of a (usually) big river (cf. Figure 2.2b). The same branching pattern can be observed here as well, at different magnification levels. This interesting

(a) Fern plant with recursively repeating branching pattern, at different scales. Photo courtesy of Jonathan Wolfe.

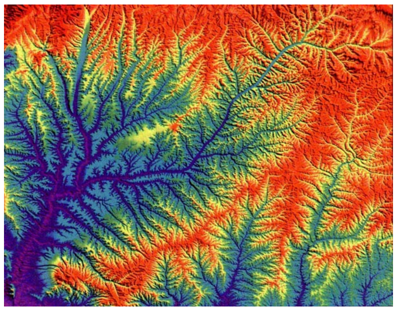

(b) Self-similar river network from the Shaanxi province in China. Scale is 300 km across. Colors represent elevation. Image courtesy of Bruce D. Malamud, Kings College London.

Figure 2.2: Different fractal behaviour in nature

behavior was studied by Leonardo da Vinci, long before it was all turned into a science. He observed that all the branches of a tree, taken at a particular height along an arc, when put together, have the same width as the tree trunk (cf. Figure 2.3). This is also applies to smaller branches that divide into even smaller twigs. In this situation each branch acts like the trunk for the smaller branches.

The human anatomy also presents some characteristic fractal patterns. For example the lung bronchioles indicate branching fractal arrangement (cf. Figure 2.4). The same behavior can be observed when looking at arteries and veins in Figure 2.5 and 2.6. The iris of the human eye is also home to some intricate designs (cf. Figure 2.7).

All the examples above can be observed at a macro level, but these designs also persist in the microarchitecture of different tissues. For example, the neural network shows a certain degree of irregularity (cf. Figure 2.8). The same is true for the TB, the test subject of the VOT algorithm, which will be presented later in Chapter 4 (cf. Figure 2.9).

As stated in Chapter 1, the TB features all fractal properties from *P1* to *P5* to be suited to undergo a fractal analysis such as VOT. 'The main tool used to describe the fractal geometry and the heterogeneity of irregular shapes' ([LB09, p. 635]) is called *fractal dimension - FD (fractional, as in Mandelbrot's early studies - [Wol67])*, which will be explained in the next Section. Therefore, the goal for algorithms like VOT is to find the best possible approximation for the FD of a fractal surface. Usually, the FD is a very sought-after parameter in the image analysis in the medical field.

2.3 Fractal dimension vs. topological dimension

In Section 2.1 the properties of fractals were listed and illustrated. However, property *P4* was set aside due to the impossibility of explaining it in pictures. This property says that an object is considered a fractal if (among other) its fractal dimension (also known as Hausdorff-Besicovitch dimension D_h) is greater than its topological dimension (D_t). Lopes and Betrouni define the two as following [LB09, p. 635]:

Definition 1 *The Hausdorff-Besicovitch dimension D_h is defined as the logarithmic ratio between the number N of an object's internal homotheties and the reciprocal of the common ratio r of this homothety:*

$$D_h = \frac{ln(N)}{ln(\frac{1}{r})} \tag{2.1}$$

Definition 2 *The topological dimension D_t of an object corresponds to the number of independent variables needed to describe it. Thus, a point is 0-dimesional, a curve is 1-dimensional, a plane is 2-dimensional, and in general an Euclidean space R^n is n-dimensional.*

Definition 2 does not require any further explanations and definition 1 can be easily understood with the help of a straightforward example: the *von Koch snowflake curve*, a simple geometrical fractal.

In Figure 2.10, if we look at the first triangle segment-wise, we see that in the next iteration each and every segment has turned into 4 smaller segments, each of those being only $\frac{1}{3}$ of the original one. In this case, 4 will be N, the number of internal homotheties (irregularities) and $\frac{1}{3}$ will be the ratio of each homothety to the original parent. This gives a fractal dimension of $D_h = \frac{ln(4)}{ln(\frac{1}{\frac{1}{3}})} \approx 1.26$. This is a non-integer value, while the topological dimension is always an integer. The non-integer value of 1.26, 'greater than one but less than two, reflects the unusual properties of the curve. It somehow fills more space than a simple line ($D_t = 1$), but less than an Euclidean area of the plane ($D_t = 2$)' [PSB88, p. 28]. In the same manner, to a 2D (in terms of topological dimension) fractal

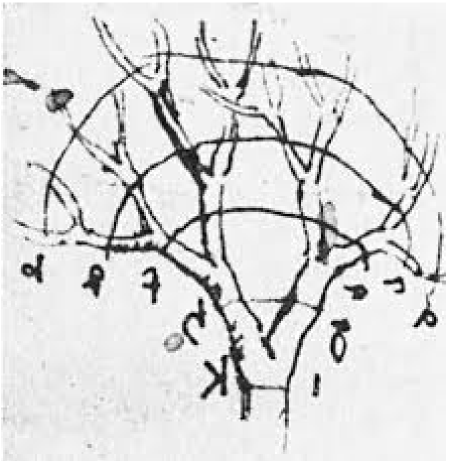

Figure 2.3: Sketch from Leonardo da Vinci's notebooks representing his observations on the fractal pattern of the tree branches. Source: Google Images.

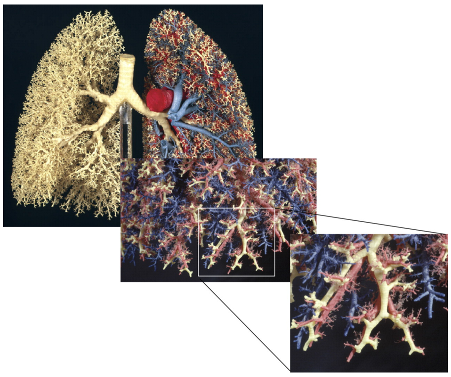

Figure 2.4: Branching fractal pattern in the bronchial tree. Photo courtesy Ewald Weibel, Institute of Anantomy, University of Berne.

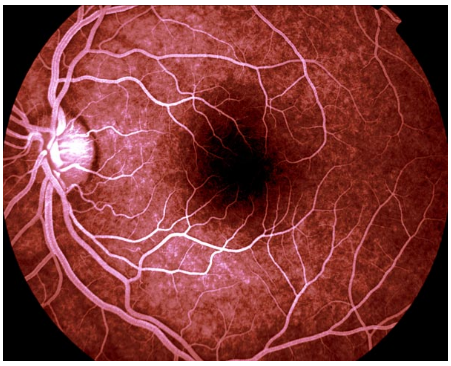

Figure 2.5: Branching fractal pattern in the vessels within the human retina. Image courtesy of Paul van der Meer.

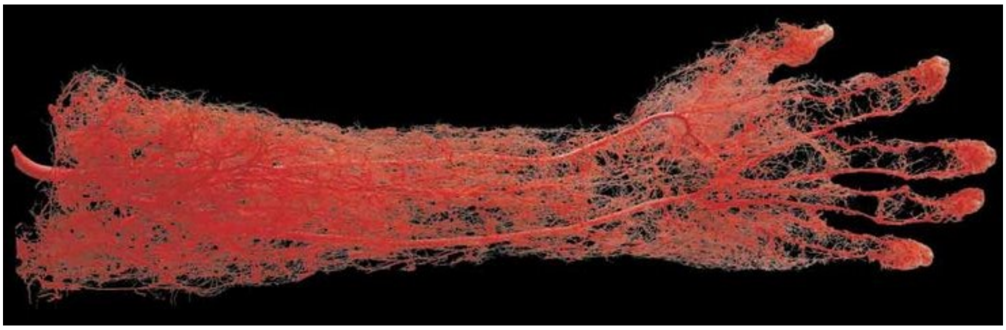

Figure 2.6: Branching fractal pattern in the vessels within the human hand. Source: Google Images.

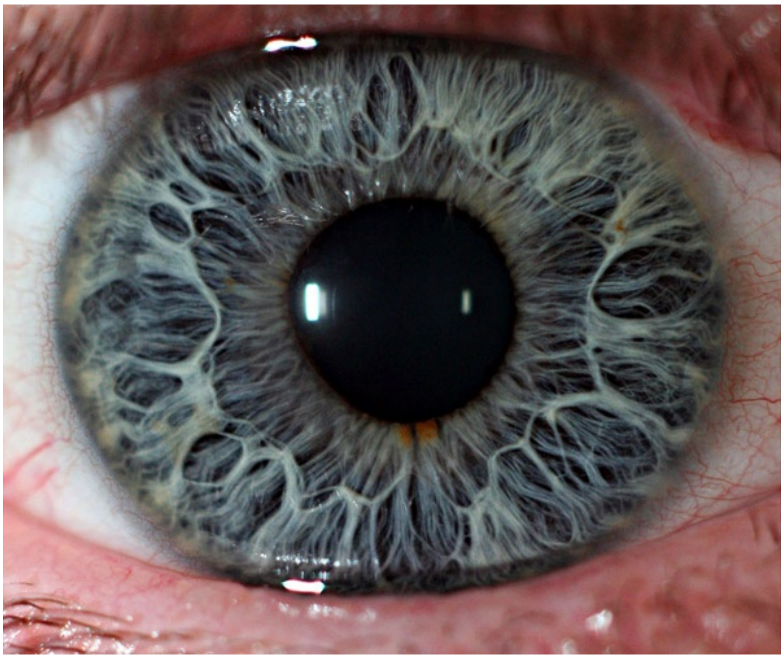

Figure 2.7: Human eye iris showing peculiar arrangement of the stroma. Source: Google Images.

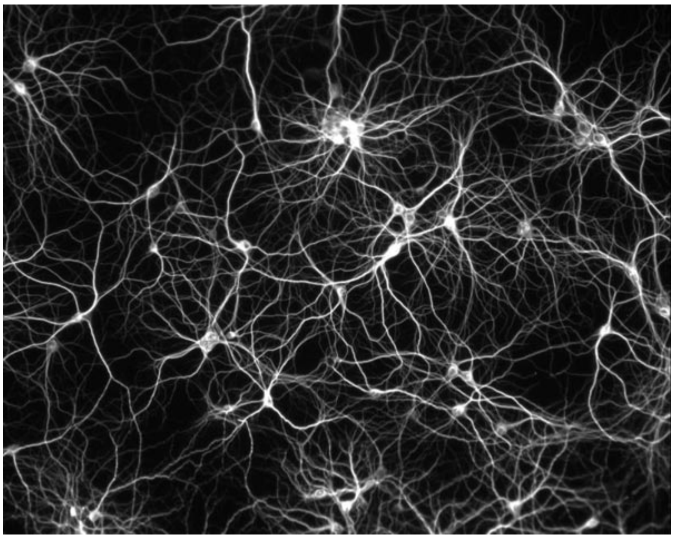

Figure 2.8: Hippocampal neurons. Scale approximately 700 microns. Image courtesy of Paul de Koninck, Universite Laval.

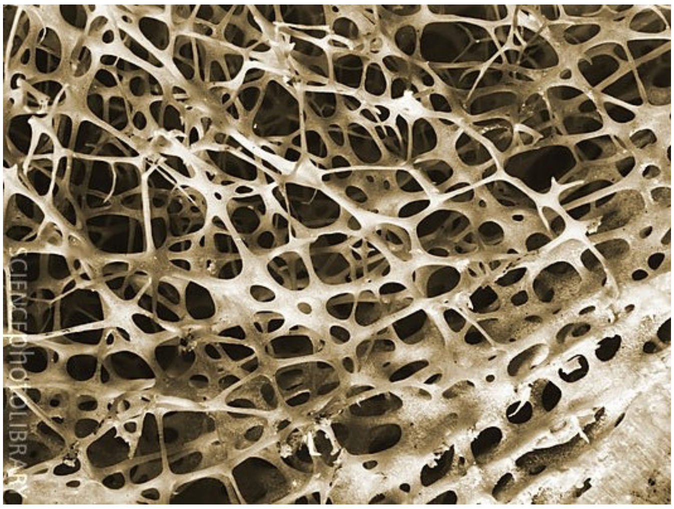

Figure 2.9: Subchondral trabecular bone - microarchitecture. Source: Science Photo Library (www.sciencephoto.com).

surface, a fractal dimension between 2 and 3 will be attributed. This is the case of the TB, as we will see in Chapter 4.

To summarize the message of this section, the fractal dimension 'allows capturing what is lost in traditional geometrical representation of shapes. In Euclidean geometry, topological dimensions (D_t) of shapes remain constant and do not provide detail about the irregularities attached. For instance, in (only) 1D, D_t is unable to distinguish a straight line and a crooked line' [LB09, p. 635]. At the same time, a 2D system would be

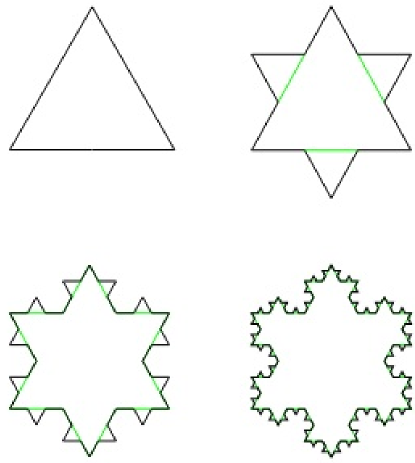

Figure 2.10: The first four iterations of the von Koch Snowflake

too much to describe it, so there must be something in-between; that 'in-between' is the fractal dimension of a certain object and it is a measure of how irregular that object is.

Usually, in medical image analysis, the fractal dimension of a surface is not directly calculated, but a (or more in case of VOT) so-called *Hurst coefficient* is found first, which is directly related to the sought fractal dimension, as it will be shown in the following sections.

2.4 Hurst coefficient

The *Hurst coefficient* (also known as *Hurst exponent*) is a very important parameter in the study of fractal geometry. The idea behind it stems from another interesting field of study, namely hydrology. This term came into being while Harold Edwin Hurst, as a lead researcher, was studying the optimum dam sizing for the Nile river [Hur51] [HBS65]. The rain and drought cycles around the river basin were exhibiting some sort of randomness or 'chaotic' behavior, meaning that they could not be efficiently and consistently predicted. Thus, the *Hurst exponent* was introduced and it tried to bring some 'order into chaos'.

Statistically, the Hurst coefficient is a measure of *long-range dependency*[1] of *time series*[2] (the radiograph of a TB can be seen as a 2D time series with different intensities at different points 'in time'). Therefore, the Hurst exponent is a global property of a

[1] also known as *long-range memory, long memory or long-range persitency* - a term that arises when studying the decay of statistical dependency (autocorrelation) of two or more measurments with increasing time between the measurements

[2] a sequence of data points that come out of successive measurements at different but equally-spaced time intervals

process, while the fractal dimension is only a local property. For self-similar processes (applicable for TB, as already presented in Chapter 1), 'the local properties are reflected in the global ones, resulting in the celebrated relationship' [GS01, p. 1]:

$$D = n + 1 - H \tag{2.2}$$

where n is the topological dimension of the surface in discussion. This means that in the case of the TB:

$$D = 3 - H \tag{2.3}$$

where n was replaced by 2.

The H parameter was first introduced to the field of fractal geometry by Mandelbrot [MWC68], who was inspired by the studies of Hurst. It was shown to indicate a 'mild' (positive correlation between measurements at different time points in a process) or 'wild' (negative correlation) randomness [MH05], depending on its value. As the H parameter can take values between 0 and 1, a value smaller than 0.5 represents a 'wild' randomness and a value bigger than 0.5 represents a 'mild' randomness. This makes sense when checking the statements with equation 2.3: a value of H closer to 0 would mean an overall D with a value very close to 3, meaning that the surface is so complex that there are almost 3 dimensions required to describe it. The surface is said to be 'rough'. On the other hand, when the H is closer to 1, the D would get closer to 2, meaning that the fractal surface is not very fragmented and 2 dimensions would suffice to describe it, i.e. the surface is said to be 'smooth' in this case.

When applying the observations above to the 2D projection of TB, a 'mild' randomness (H between 0.5 and 1) corresponds to a healthy bone, whilst a 'wild' one (H between 0 and 0.5) would correspond to a more damaged/rougher bone. The latter is perhaps due to the early effects of the OA within the TB.

The goal of the VOT algorithm is to find this so-called *Hurst coefficient* and together with it also the fractal dimension of the TB projection. VOT belongs to the class of fractal methods when speaking of medical image analysis, because it makes use of all the principles and properties of fractals presented in previous sections. There are also non-fractal methods that produce fair results. The difference between the two will be illustrated in the next Chapter. In the same Chapter state-of-the-art methods for assessing TB and grading of OA will be presented as well.

CHAPTER 3

State-of-the-art and similar approaches

Normally, in daily clinical practice, the OA within the knee is found and assessed by calculating JSN (joint space narrowing — Figure 3.1) and by observing the development of osseous cysts (Figure 3.2) and osteophytes (Figure 3.1) on the surface of the bone within the joint. This information is extracted from knee plain radiograph since it is the cheapest imaging technique. Other strong indicators of OA, which can also be seen in the radiographs include: increased density of the subchondral bone (sclerosis — Figure 3.1) and bony remodeling (due to the attempt of the bone to repair itself). All the above-mentioned parameters can either be visually quantified by a specialist or there exist special decision support systems that do an automated quantification and return a human-readable report.

Figure 3.1: Reduced medial JSN, sclerosis and osteophyte formation due to OA. Source: `http://stemcelldoc.wordpress.com/2011/11/16/knee-osteoarthritis-grading-limitations-of-x-rays/`.

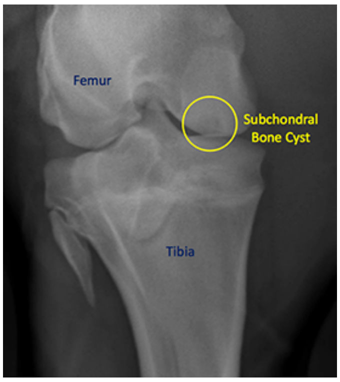

Figure 3.2: Bone cyst formation due to OA. Source: Google Images.

Once the possible indicators of OA are assessed, a grading of the affection is decided based on the so-called *K-L system* (Kellgren–Lawrence grading scale) [KL57]:

Grade	**Description**
0	No radiographic features of osteoarthritis.
1	Possible joint space narrowing and osteophyte formation.
2	Definite osteophyte formation with possible joint space narrowing.
3	Multiple osteophytes, definite joint space narrowing, sclerosis and possible bony deformity.
4	Large osteophytes, marked joint space narrowing, severe sclerosis and definite bony deformity.

Table 3.1: Different grades of OA after KL scale.

Even though the mentioned method for discovering and grading of OA was proven to be consistent over a very long period of time, it has been criticized for not being accurate enough to discover the early impacts of OA on the TB, such as the thickening and tendency for vertical alignment of the trabeculae.

In the field of medical image analysis there have been several methods developed that take radiographs as input and return different meaningful texture parameters. Most of the methods are also applied to the TB. There are non-fractal, as well as fractal approaches (such as VOT) being used, investigated and further improved at the time of writing this work.

3.1 Non-fractal methods

This class of methods analyze a radiograph by extracting other possibly interesting bone surface features, in a lot different manners.

3.1.1 Co-occurence matrix

A co-occurrence matrix can be computed for each and every possible image of size $n \times m$ after the following formula:

$$C_{\Delta x,\Delta y}(i,j) = \sum_{p=0}^{n}\sum_{q=0}^{m}\begin{cases}1, & \text{if } I(p,q) = i \text{ and } I(p+\Delta x, q+\Delta y) = j\\ 0, & \text{otherwise}\end{cases} \tag{3.1}$$

where $C(i,j)$ is the $(i,j)^t h$ entry in the co-occurence matrix, p and q are spatial coordinates in the image and $I(p,q)$ is the intensity of the pixel found at position (p,q) in the image. Δx and Δy are given offsets for x and y coordinates which depend on a direction and on a distance. C is a square matrix having its dimension the number of intensities found in an image.

Basically, equation 3.1 says that each entry in the co-occurrence matrix will be occupied by the number of pixel pairs from the original image for which the following are true (number of co-occurring intensities at a given offset):

1. The intensity of the first pixel from the pair is equal to i, i.e., the number of the current row in the co-occurence matrix.
2. The intensity of the second pixel from the pair is equal to j, i.e., the number of the current column in the co-occurence matrix.
3. The two pixels have a certain given distance between them.
4. A line passing through the pair of pixels makes a given angle with a horizontal reference line.

As an example [V12, p. 153], for the following RGB image, consisting of intensities with values $0, 1, 2, 3$:

$$R = \begin{bmatrix}0 & 0 & 1\\ 0 & 1 & 2\\ 0 & 2 & 3\end{bmatrix},\ G = \begin{bmatrix}1 & 2 & 3\\ 0 & 2 & 3\\ 0 & 1 & 2\end{bmatrix} \text{ and } B = \begin{bmatrix}1 & 3 & 0\\ 0 & 3 & 1\\ 3 & 2 & 1\end{bmatrix}$$

the co-occurrence matrix would have the following form when computed for the given direction of 0 degree (i.e. horizontal direction) and distance of 1:

$$C = \begin{bmatrix} 1 & 3 & 2 & 1 \\ 0 & 0 & 3 & 1 \\ 0 & 1 & 0 & 3 \\ 1 & 1 & 1 & 0 \end{bmatrix}$$

This means that for example there is only 1 ($C(0,0) = 1$) pair of pixels of intensities 0 ($i = 0$) and 0 ($j = 0$) which are neighbors (distance 1) and which lie horizontally to one another (direction 0 degree). This is true, the only such pair being in matrix R on positions $(0,0)$ and $(0,1)$.

The co-occurence matrix is a measure of texture and it is often used in medical image analysis. Usually because these matrices are extremely big and therefore sparse (meaning that they contain relevant information only in pathces, since, for example, a 16 bit deep gray level image will generate co-occurence matrices of sizes $2^{16} \times 2^{16}$), certain metrics of the matrices are often extracted that lead to a more useful, describing set of features for the texture. These features are referred to as *Haralick features* (also known as statistical measures) and among them are [HSD73, p. 619]:

Measure	**Description**
Contrast	A measure of local variations in the original image.
Correlation	Measures the joint probability occurrence of the specified pixel pairs.
Energy	Equal to the sum of the squared elements in the co-occurence matrix. It is also called *uniformity* or *angular second moment*
Homogenity	Measures the distribution of elements in the co-occurence matrix to the main diagonal.
Entropy	Measures the degree of randomness in the signal.

Table 3.2: Some Haralick features.

3.1.2 Line Fraction Deviation (LFD)

LFD is a texture algorithm that was designed to find main orientation within structures. Given the particular construction of the TB, with trabeculae oriented after stress distribution within bone, the algorithm is generally used to assess the dominating orientation of the trabeculae inside the TB, as it can be a strong indication of different bone deformations.

For the assessment, radiographs of TB are acquired. Over each radiograph's center a mask will be placed. Because this mask needs to be rotated to find a so-called *LFD* *index* for different directions, the mask needs to be smaller than the original radiograph. This is to guarantee that during the rotation the mask remains within the boundaries of the radiograph. Usually the selected region of interest (ROI) from the radiograph is of size 256×256 and the mask is chosen to be 180×180. This means that the said mask will consist of 180 adjacent lines, each of them consisting in turn of 180 pixels. At first, the grid is placed with its edges parallel to ROI's edges and for each line within the grid, the ratio of bright pixels to the dark pixels is saved. After all lines are analyzed, there will be 180 ratios saved. Out of these ratios a SD (standard deviation) is calculated, which is the needed LFD index. At the end the grid is rotated and the calculations are repeated to yield LFD indexes in different direction. For a simple illustration of the process, see Figure 3.3. At the very end, after every desired direction is analyzed, a rose plot of orientation is drawn, its peaks indicating the dominant orientation of the bone structure.

The algorithm was developed as a replacement for an older one, called *mean intercept length(MLI)*, which works in a very similar way, but instead of calculating ratios, it only stores the number of intersection of the mask's lines with bright and/or dark pixels. The area of the ROI is divided through the obtained number and the result is the MIL. The MIL usually produces elliptical plots with not much information regarding the texture, while LFD appears to be sensitive to anisotropy and thus much more useful.

A possible problem with this algorithm is that even though it is able to work directly on radiographs, for good accuracy the image has to be binarized, which can lead to some degree of information loss.

3.2 Fractal methods

Since it has been proven that the TB exhibits clear fractal properties [FP96], the fractal methods for describing TB texture have gained more attention lately. In the following subsections some popular fractal methods will be described shortly. The disadvantages of those methods that led to the development of VOT will also be pointed out.

3.2.1 Box-counting Method(BC)

There are three main variations of the box-counting algorithm, but they all work under the same principle with some slight modifications and adaptions.

The simple box-counting method lays, in turn, square boxes of different sizes r over a ROI and counts how many boxes are needed to cover the entire signal. Usually r is chosen as small as computationally possible and every reiteration is decreased even more (cf. Figure 3.4). After a given number of reiterations is completed, the values that represent the number of boxes are plotted versus the different corresponding box sizes. A linear regression is fitted on these data points and the slope of the line will be a approximation of the FD (fractal dimension) of the TB surface.

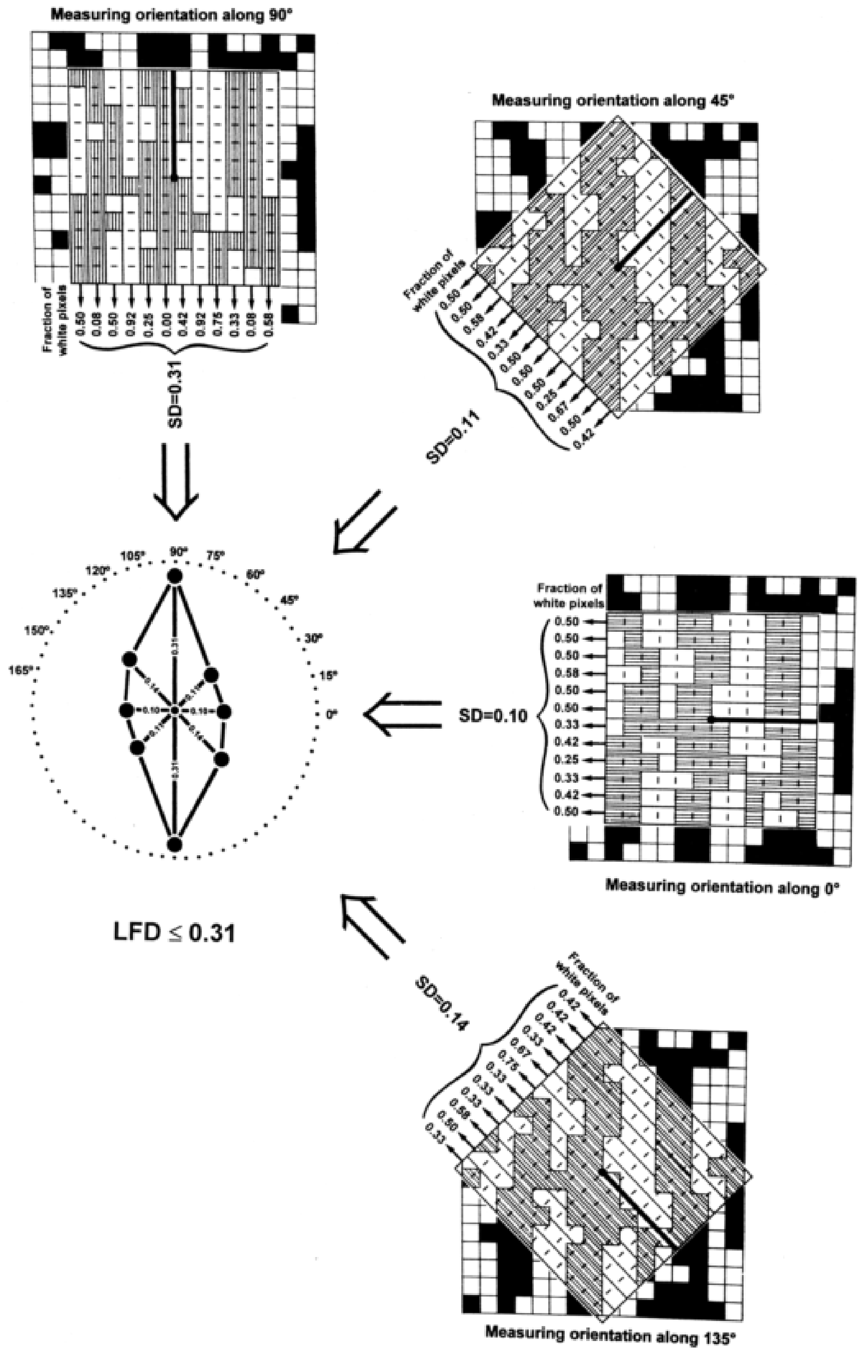

Figure 3.3: Illustration of LFD algorithm. Figure and explanations taken from [Ger98, p.384]

The main drawback of this method is that it can only work with binarized signal [LB09]. As a consequence, information loss is almost always imminent.

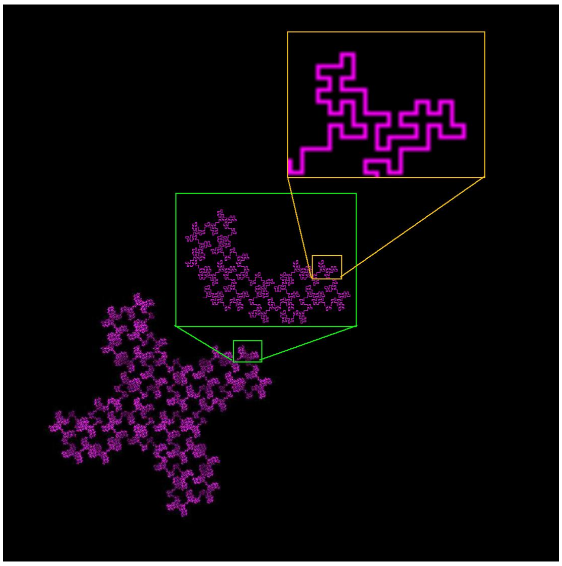

Figure 3.4: Illustration of how the BC algorithm is chosing smaller and smaller boxes. Image courtesy of Wikipedia Creating User 'Akarpe': `https://en.wikipedia.org/wiki/Box_counting#/media/File:32_segment_fractal.jpg`.

3.2.2 Differential Box-counting Method(DBC)

In contrast to BC method, DBC is able to work with untouched, unprocessed radiographs of the TB. Therefore, binarization is not needed anymore and the information loss can be avoided, the analysis being thus possible directly on the gray scale image.

The difference from the original BC method lies only in the different partitioning of the image. Here, the entire image is partitioned in blocks of a given size r and on each such block, 3D columns composed of boxes of sizes $r \times r \times r'$ are laid, where r' is the height of each box which depends on the number of total gray levels present in the image. The height of the column also depends on the number of intensities available in the radiograph. Each box in the column is numbered and the boxes where the minimum and maximum intensities lie are found. This is possible if one imagines that the image would have a third dimension which represents the intensity levels and which can be imagined to be parallel to the box columns, upwards (cf. Figure 3.5 as an example with boxes with size $3 \times 3 \times 3$ and underlying blocks of size 3×3). The difference between the maximum and the minimum are computed and stored for each block. For example, in Figure 3.5, the minimum is within Box 1 and the maximum is within Box 3, meaning that the difference will be $3 - 1 = 2$ in this case.

After all the differences are available, they are summed together and then the size of the block is reduced/increased and the calculations are reiterated a desired number of times. With different sums of intensity differences and different block sizes, a plot similar to the one in Section 3.2.1 is drawn, a linear regression is computed and the slope of that line is the FD of the surface. Even if this method is one step in front of the last one, it is still faulty for it was proven that it usually underestimates the FD. [LCW+14].

3.2.3 Extended-counting Method(XC)

In this case, the entire image is divided into further subsets for which the algorithm from Section 3.2.1 is applied, the only difference being that for every subset, only two different box sizes are used. This will produce a FD for each subset and the maximum FD among the subsets is chosen as the general FD of the surface. Other than being able to run only on skeletonized (binarized) images, this method was found to overestimate the FD [LB09, p. 636].

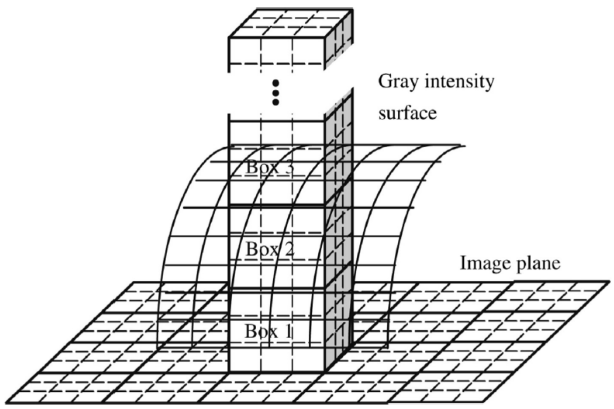

Figure 3.5: Sketch of DBC selecting blocks and boxes [LDS09].

3.2.4 Triangular Prism Method(TPM)

This particular method of finding the FD of a fractal set/surface is different from the fractal methods mentioned before in that it uses so-called *intensity area measurements* to find an approximation for the FD.

At first, a square mask of given size r is placed over the signal. The four corners of the mask will fall on certain pixels of certain known intensities. These points are viewed as *terrain elevation*. The center of the square will also have an attributed elevation (intensity), which will be the mean of the surrounding elevations. All the corners will be connected to this mean elevation and thus triangles of different inclinations will be formed. The entire structure in a prism (cf. Figure 3.6).

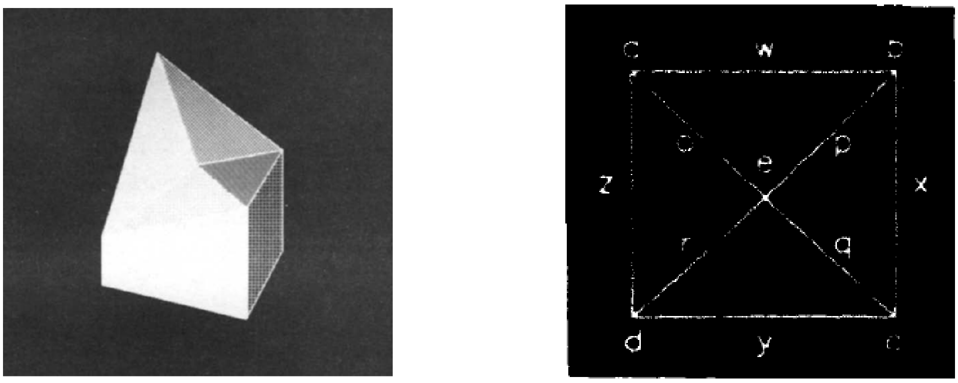

(a) Prism viewed from the side. (b) Prism seen from above.

Figure 3.6: Created prism after connecting terrain elevations [Cla86].

Next, using Heron's formula the entire surface area (the sum area of all the triangles formed) of the prism is calculated.

At the end, the process is reiterated by increasing/decreasing the base size r and after a given number of iterations, the obtained total surface areas are plotted against the base sizes. The data is fitted with the best fitting line based on least squares principle and the slope of this line corresponds directly to the FD of the fractal set [SFQ97]. Even though the method was found to be the fastest in its class of area calculation methods, it was also proven that it underestimates the FD and it is very sensitive to noise and extreme grey-level values [LB09, p. 637].

CHAPTER 4

Variance Orientation Transform

4.1 Motivation

As stated in Chapter 3, most of the methods intended for the analysis of TB surface that were developed prior to VOT only calculate a single FD as the representative value for the entire bone surface. This was proven to be just a limited indicator of the complexity of the TB, compared to how much information the 2D radiograph holds in reality.

In 2001, Keaveny et. al. [KMNY01] showed that the TB is of anisotropic nature, meaning that its characteristics are changing with the direction in which the signal is analyzed. This observation rendered the previous fractal methods obsolete, when applied to TB. Moreover, in Section 2.2 it was already mentioned that the TB indicates strong fractal properties. This fact is of crucial importance since 'a fundamental characteristic of fractal objects is that their measured metric properties, such as length or area, are a function of the scale of measurement' [LB09, p. 634]. Indeed, it was shown that TB changes not only with direction, but also with the scale [PF00, MKA+98].

There are at least two attempts to cover the shortcomings of the already available algorithms: *fractal signature analysis (FSA)*[MWTBW05] and *Augmented Hurst Orientation Transform (AHOT)* [PLDS08]. The problem is that these two methods only calculate *fractal signatures* (i.e. FD over individual scales) in horizontal and vertical direction, i.e. 0° and 90°. In 2008 Wolski proposed a fix for this problem — *Variance Orientation Transform* [WPS09]. VOT is able to find more FDs, over a wide range of scales, along every possible direction. In the following sections our attempt at implementing of VOT will be described in more detail.

4.2 Surface representation

First, a number of mathematical notations must be introduced. A 2D bone radiograph is saved in digital format in form of pixels, each having a different intensity value attached to it. Thus, an image is digitally represented by a matrix of size $N_x \times N_y$, where N_x and N_y are the number of pixels in the horizontal and vertical directions respectively (i.e., the numbers of columns and rows of the matrix). This means that the spatial coordinates x and y can take following values: $x \in \{0, 1, ..., N_x\}$ and $y \in \{0, 1, ..., N_y\}$ with any pair (x, y) coding for a position in image. Note that since this attempt at implementing VOT was first done in Matlab R2013b, the indexing begins at 0. Further, because the intensities of each pixels must also be coded somehow, another set, the data value range, must be introduced: $z \in \{0, 1, ..., N_z\}$ with N_z being the maximum number of intensities that can be represented within a particular image. For example, in case of a 16 bit pixel encoding, each pixel can have an intensity between 0 and 2^{16-1}. In short, as Wolski says [WPS09, p. 212], the image can be seen as 'a function which assigns a brightness value z to a pixel location (x, y), i.e. $z = I(x, y)$'.

4.3 Preprocessing

As with every data acquisition technique, radiography is prone to many type of noises which can stem from different sources Almost every element of the system can be a noise generator [SH00]. It is thus important to reduce any noise as much as possible because otherwise the calculations within the algorithm can be affected and the end result could vary too much from reality. In the present approach at implementing the VOT algorithm, two methods were investigated for filtering out the unwanted noise.

First method was proposed by Podsiadlo et al. [PSD+10, p. 324]. This method removes high and low frequency noise in the following manner: the high frequency noise is reduced by applying a 5×5 median filter; the low frequencies are diminished by a technique called *background image subtraction*, as follows. First, an average filter is applied in order to obtain a smooth, low-frequency image. Second, this newly-created low-frequency image is subtracted pixelwise from the original image (the one that the median filter has already been applied to).

With this work we propose our own method for filtering which involves eliminating all pixels that lie outside a certain number of SDs (standard deviations) in the intensity distribution of the image. To achieve this, first a blurred image is obtained by applying a median filter. Second, the blurred image is subtracted pixelwise from the original image and the SD is calculated for the result image. Third, the pixels in the image where the difference is bigger than $6 \times SD$ are marked as 'hot' or 'cold' pixels (depending on which side of the distribution they appear). Finally, all the intensities of all the marked pixels are replaced by the corresponding values (from the same spatial coordinates) from the blurred image.

Normally, the appropriate filter does not affect the features of the image we are interested in. Thus, the output of consecutive filtering should be the same as the original image in case there is no noise. Judging by this criterion, the second method has proven to be better, as the results only differ in the order of 10^{-3} in terms of calculated FD, whereas when applying the first method, the results indicate considerable changes in the order of 10^{-1}, which can have a serious effect on the interpretation of the results. This is because the calculated *Hurst coefficient* lies in interval $(0, 1)$, with the first decimal point being the most meaningful; the decision whether the image is smoother or rougher is drawn after the first decimal point (greater or smaller than 0.5).

An example of a noisy image can be seen in Figure 4.2. This ROI was extracted from a knee radiograph from within the medial part of the TB (cf. Figure 4.1). In Figure 4.3 one can see the image after the proposed filter was applied. It is clearly visible that many 'hot' (white) or 'cold' (black) pixels that are present in the original image, can no longer be observed after the operation is done. This kind of filtering can not only be used with TB, but with any radiograph that is susceptible to noises such as salt and pepper noise.

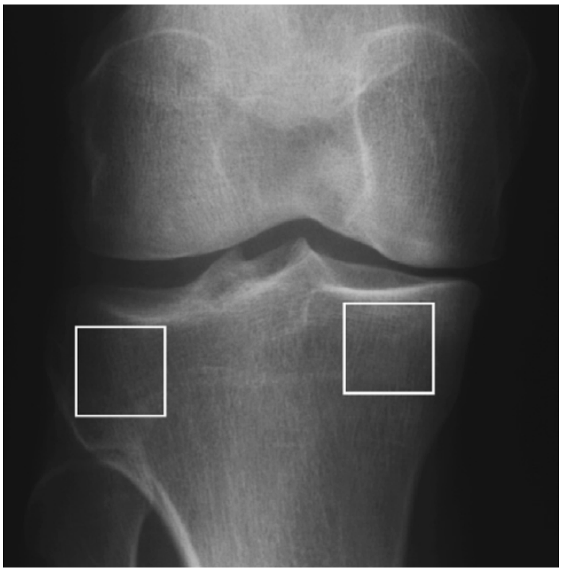

Figure 4.1: Knee radiograph with markings for to-be-extracted ROIs. The left box is placed within the lateral TB (one can deduce that because of the presence of the fibula in the lower left corner) and the right box within the medial. Image taken from [PSD+10, p. 325]

After the filtering is done, the image is ready to be processed with the VOT algorithm.

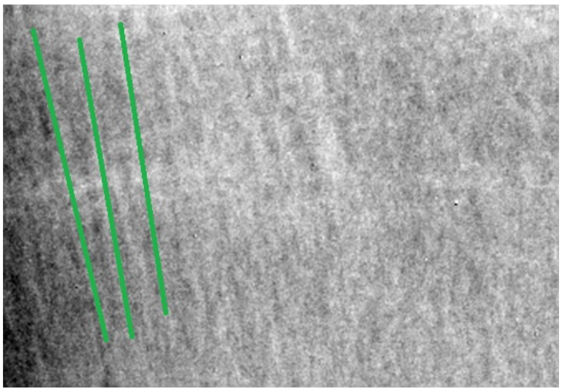

Figure 4.2: Noisy image of medial TB

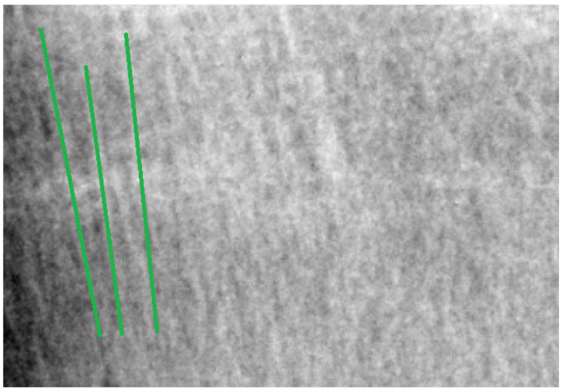

Figure 4.3: Filtered image of the same medial TB. The clarity of the image seems slightly distorted (blurred) to the human eye but the structure (the position and orientation of the trabeculae — green) is not affected.

4.4 The Algorithm

This Section covers the detailed description of our attempt at implementing the VOT algorithm, which was first described by Wolski [WPS09]. For a better overview of the entire process a simplified sketch can be seen in Figure 4.7.

Step I. A circular, or rather a ring mask is defined as the search region of the algorithm. This ring has the inner radius of four pixels and the outer radius of 16 pixels. The search region is forced to be completely inside the image by skipping the pixels that are too close to the borders. This is to make sure that the bottom half of the search region is within the limits of the imagen and thus the calculations remain consistent. Using a predefined set of directions (in this case 24 directions, i.e. every 7.5° in range $[0, \pi)$), differences between intensities of each pixel along each direction and the center of the search region are calculated and saved (the pixels along each direction are discovered by means of the Bresenham's algorithm). Along with these differences, Euclidean distances of all pairs are also calculated and stored in an appropriate matrix R where the columns represent increasing Euclidean distances (image sizes) from the center of the search region and the rows represent different directions. Note that the pairing with the center of the search region is done only for pixels that lie between the two defined radii (cf. Figure 4.4).

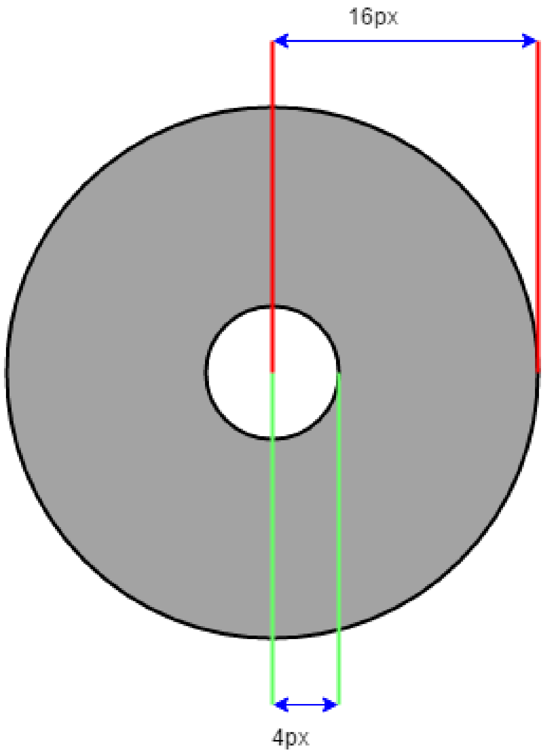

Figure 4.4: VOT search region. Only the pixels that lie in the grey region will be considered for the calculations.

Step II. The algorithm checks if along every considered direction, the maximum possible number of pixels was discovered (i.e. the number of pixels in the horizontal direction or 0°, which is $16-4+1=13$ pixels, because the pixels lying on the inner radius are excluded, but the ones lying on the outer radius are included). If there are directions along which less than 13 pixels were discovered, a second attempt at 'completing' these directions is made as follows:

1. A direction that was found to not have 13 pixels is selected.

2. A line is drawn along that certain direction.

3. The line is equally spaced obtaining 13 different points with real coordinates $(a_1, b_1), (a_2, b_2), ..., (a_{13}, b_{13})$ (cf. Figure 4.5). These points represent the locations of possible pixel candidates. The candidates are found as follows:

   3.1. The first point P_1 of coordinates (a_1, b_1) is selected and its 'host' pixel C is found by rounding its coordinates.

   3.2. Around the host pixel a 3×3 neighborhood is considered.

   3.3. All the pixels in the neighborhood are sorted in ascending order by their Euclidean distance to point $P1$.

   3.4. Every pixel is taken in turn and it is checked whether it has been previously found to belong to the current direction or to any other direction.

   3.5. If a pixel is found to be valid (not member of any other direction yet) its information (intensity difference with the center of the search region and the Euclidean distance to the center of the search region) is added to the current direction in the set R.

   3.6. The process is repeated with the rest of the real points until the required number of valid pixels (13) is found or until reaching the end of the equally-spaced line with not enough pixels. If the latter is the case, the direction is discarded from further calculations.

4. The entire process is repeated until there are no directions left.

It is important that along all directions (after discarding the invalid ones) the number of pixels is the same, otherwise the simulation of scales would not be possible later in the algorithm. The reason why in *Step I* the angle between adjacent directions was chosen to be 7.5° is because before starting the algorithm it is not known how high is the maximum number 'valid' (with 13 pixels) independent directions. Therefore, the assumption that the minimum angle between two independent directions is 7.5° is made and through the pixel inclusion or direction selection process presented in *Step II*, 'invalid' directions are discarded from any further calculation. This way the maximum possible number of independent beams (directions), for a search region of dimensions presented in *Step I*, is forced.

Step III. The search region moves one pixel to the right and steps I and II are repeated. The whole process is repeated until the search region reaches the end of the image (bottom-right corner). Note that the search region only stops on pixels where its lower half is completely inside the image. The calculations are only done for the lower half of the search region because the other directions are equivalent (270° is the same as 90°, 0° is the same as 180° and so on). While the search region analyzes the whole image, the newly-found differences between center and each pixel within the region are stored together with the older ones.

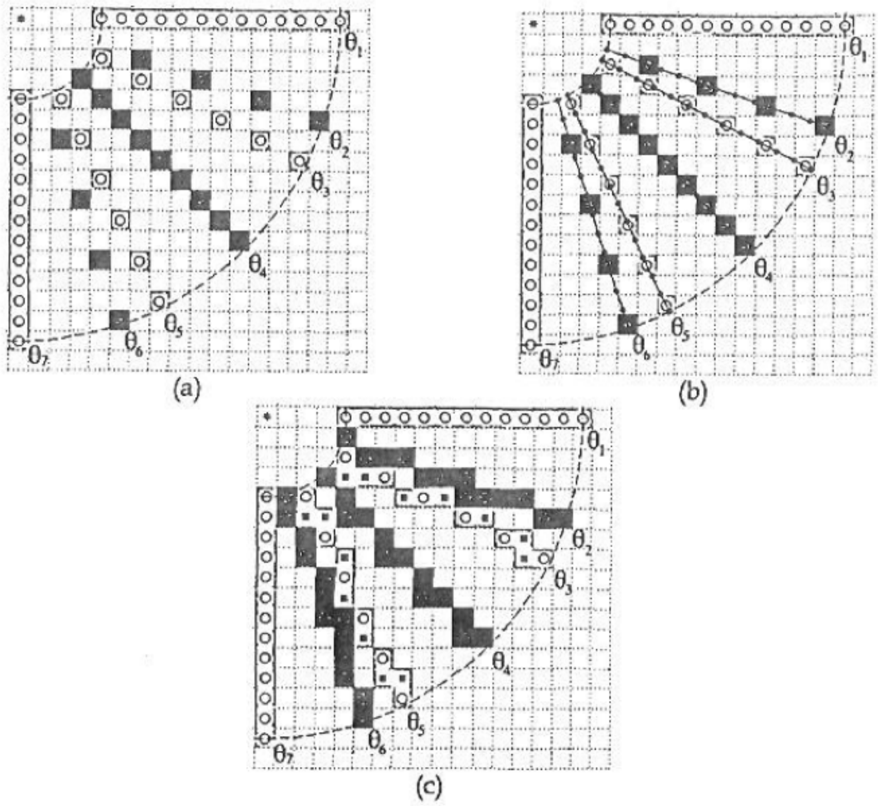

Figure 4.5: (a) set of pixels that are found along some directions before the enrichment step. (b) lines drawn along the directions with a view of finding candidates to complete the needed number of pixels (13). (c) the complete set of pixels that contain both the originally-found and newly-found pixels. Sketch taken from [WPS09, p. 215]

Step IV. All calculated differences and Euclidean distances are saved in form of a matrix as follows:

$$R = \begin{bmatrix} r(d_{11}, \theta_1) & r(d_{12}, \theta_1) & \dots & r(d_{1,13}, \theta_1) \\ r(d_{21}, \theta_2) & r(d_{22}, \theta_2) & \dots & r(d_{2,13}, \theta_2) \\ \vdots & \vdots & \ddots & \vdots \\ r(d_{N_d 1}, \theta_{N_d}) & r(d_{N_d 2}, \theta_{N_d}) & \dots & r(d_{N_d 13}, \theta_{N_d}) \end{bmatrix},$$

where N_d is stands for the number of directions that were found to be able to have 13 pixels, d stands for Euclidean distance and θ stands for direction. Thus, as already mentioned in *Step I*, each row in the above matrix corresponds to a direction and each column to a image size (13 pixels along each direction, i.e. 13 Euclidean distances to each of them, i.e. 13 image sizes). The value $r(d_{11}, \theta_1)$ represents, for example, the first position (pixel) along the first considered direction (0°). At the end, after the search region is done moving, this entry (and the other as well) contains the Euclidean distance to the first position along the first direction and all differences of intensities between the first position along the first direction and the center of the search region of all the search regions. The differences can be stored in the form of sum of differences, as the region moves across. Variances of all possible differences stored in all entries are then calculated. To achieve this, the usual variance formula has to be manipulated a bit, since in its popular form, $\sigma^2 = \frac{\sum_{i=1}^{n}(x_i-\mu)^2}{n}$, all the data is needed before being able to compute it. For speed optimizations reasons, it is faster to find a way of building the variance iteratively and not save all the differences:

$$\begin{aligned}\frac{\sum_{i=1}^{n}(x_i-\overline{x})^2}{n} &= \frac{1}{n}\sum_{i=1}^{n}(x_i-\sum_{j=1}^{n}x_j)^2\\ &= \frac{1}{n}\sum_{i=1}^{n}x_i^2-\frac{n}{n}(\frac{1}{n}\sum_{j=1}^{n}x_j)^2\\ &= \frac{1}{n}\sum_{i=1}^{n}x_i^2-\overline{x}^2\end{aligned} \tag{4.1}$$

Equation 4.1 shows that the variance can indeed be computed iteratively. This means that along with the set of differences, a second set of squares of differences must be saved at each pass of the algorithm. At the end of this step, a new matrix of the same dimensions as set R will be obtained with each entry indicating the variance of all differences that were saved for that position in the past. Another trick for speed optimization could lie in calculating Euclidean distances between pairs only once at the beginning of the algorithm. This can be done because the relative distances to the center of the ring will be always the same as it moves around. Out of the same reasons, pixel enrichment can also be done only once, because it is computationally intensive. Instead of doing it for each region position, it can be done only for the very first region found to be within the image borders. Later, the pixel coordinates (as well as the euclidean distances) can be adjusted as the region moves across (i.e. $x+1$ if the region goes to the right and $y+1$ if the search region switches a row downwards, considering that position (0, 0) in image is in the top-left corner).

Step V. After the variances for each position relative to the center of the search region are calculated and stored in the matrix, each row of the matrix will be selected in turn. Each row corresponds to a direction and it contains 13 entries (for each pixel along the direction). These 13 entries will be decomposed in 9 subsets, each consisting of 5 entries. The neighboring subsets are shifted with one entry, meaning that two neighboring subsets will have four entries in common. The Euclidean distance to the 3rd position of each subset is recorded and it corresponds to a spatial *scale* (also known as *image size* [WPS09]). If the pixel size of the image is known, then the scales can easily be calculated in millimeters. Thus, each direction will be split up into nine scales of measurement. Each subset is plotted in a log-log plot of variances versus Euclidean distances. This is done because it is assumed that the intensities in the image are generated by a fractal Brownian function, meaning that the variances of differences $VAR[|I(x+\Delta x) - I(x)|] \propto \Delta x^{2H}$, where $I(x)$ is the pixel intensity at the center of the search region, $I(x+\Delta x)$ is the pixel intensity at a distance Δx from the center and H is the Hurst coefficient [WPS14, p. 4]. If this relation is logarithmized, the $2H$ becomes the slope of a straight line that has that equation (cf. Figure 4.6). Finally, a line is fitted to the plot by means of least squares principle. The half of the slope of the fitted line represents a Hurst coefficient in a particular direction, over an individual scale. All calculated Hurst coefficients are saved in a matrix of this form:

$$H = \begin{bmatrix} H_{11} & H_{12} & \dots & H_{19} \\ H_{21} & H_{22} & \dots & H_{29} \\ \vdots & \vdots & \ddots & \vdots \\ H_{N_d1} & H_{N_d1} & \dots & H_{N_d9} \end{bmatrix},$$

with N_d being the number of directions just as with matrix R of differences/variances.

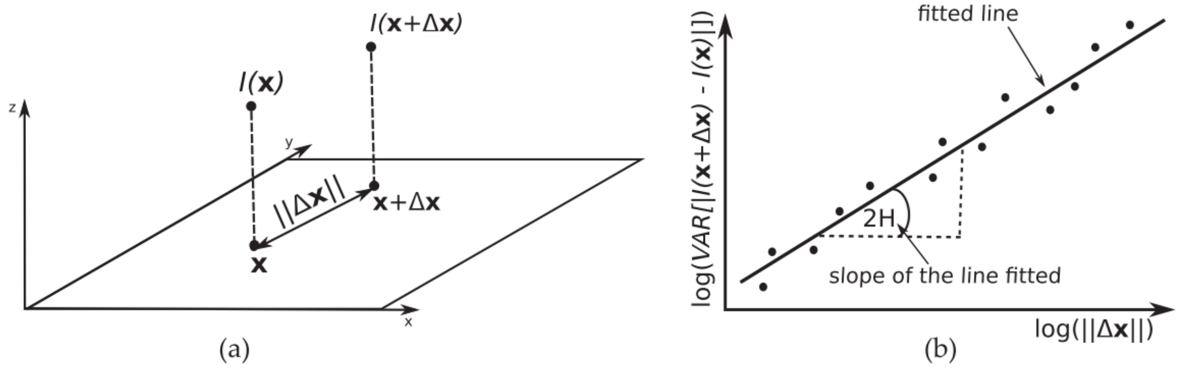

Figure 4.6: Schematic illustration of (a) the difference $I(x+\Delta x) - I(x)$ and the distance Δx, and (b) the log-log plot of variances agains distances with the line fitted and the Hurst coefficient H [WPS14, p. 4].

Step VI. Considering the same splitting technique as in *Step V*, each row of the H matrix is split into nine subsets. The subsets are grouped with the other corresponding subsets along other directions. For example, first 5 entries of each row are grouped together to form a matrix of Hurst coefficients for the first scale and so on. For each scale matrix a rose plot of orientation is drawn which indicates the anisotropy and the roughness of the surface. At the end there will be nine rose plots of orientation for each image size. To each plot an ellipse is fitted by the principles of least squares. Out of the ellipse three important parameters can be extracted [WPS09, p.220]:

1. The texture minor axis S_{ta} - a parameter describing the most significant roughness component of a surface. It is defined as half of the length of the minor axis of the

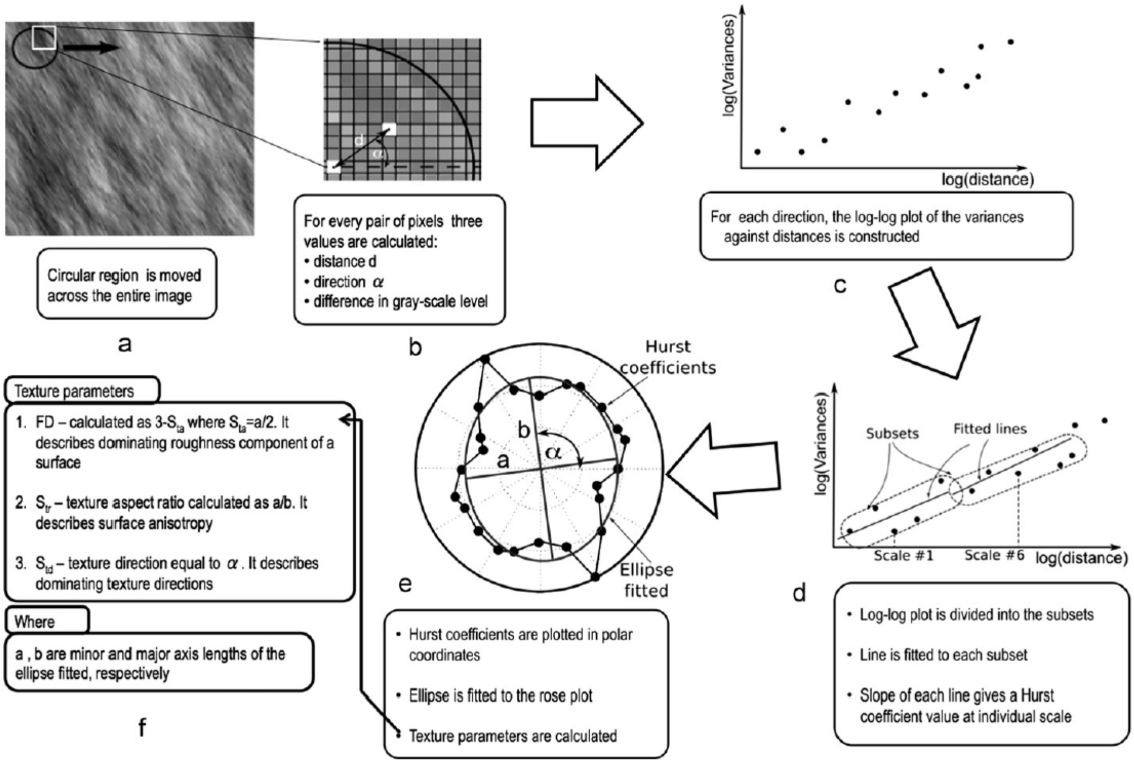

Figure 4.7: A schematic illustration of the VOT method: (a) a search region that moves across the image, (b) values calculated for a pair of pixels within the region, (c) a log-log plot, (d) lines fitted to the plot, (e) a rse plot of Hurst coefficients and (f) texture parameters calculated from the ellipse fitted. Sketch taken from [WPS10, p. 2204]

.

ellipse fitted. The S_{ta} parameter is used to calculate the FD using the formula $FD = 3 - S_{ta}$. Note that in Section 2.4 the FD was defined as $FD = 3 - H$, but in this case, S_{ta} is equivalent to a Hurst coefficient in the direction of the minor axis of the ellipse. This direction is used to calculate the most interesting FD because across the small axis the Hurst coefficient is the smallest and as it was presented in the current section, a small coefficient (that goes towards 0) indicates a rougher surface, a wilder, more random signal (together, the pixel intensities can be viewed as a discrete signal).

2. The texture major axis S_{tb} - a parameter describing the most significant smoothness component of a surface. It is an important parameter that holds information about the integrity of the trabeculae in the bone. This parameter was introduced in this list by us as we consider it of particular importance.

3. The texture aspect ratio S_{tr} measures texture anisotropy. It is defined as the ratio

of the minor axis to the major axis of the ellipse.

4. The texture direction (orientation) S_{td} indicates the dominating direction of the trabeculae of a surface. It is defined as the angle between a line parallel to the horizontal axis of the image and the major axis of the ellipse.

At the end there are nine values for each mentioned parameter, each holding information for a particular scale of measurement. There can be of course more parameters extracted. For example, a FD can be calculated in each and every direction, over each and every scale, just by subtracting the corresponding Hurst coefficient from 3 dimensions. This would yield the FSs (fractal signatures), but not all of them usually hold important information. Characteristic for the fractal surface is the largest FD that can be found, meaning that in that particular direction the structure is more complex than anywhere else in the image. The largest FD is where the Hurst coefficient is the smallest and that is always indicated by the minor axis of the fitted ellipse.

4.5 Proof-of-concept

It would be ideal if there would be some degree of certainty that the algorithm works as supposed. Fortunately, there exist techniques of generating 2D fractal isotropic and anisotropic surfaces with a given fractal dimension.

For generating isotropic fractal surfaces, a so-called *fractal synthesis technique* is used. This algorithm was developed by Saupe [PFS$^+$12, p. 108]. As a first example, a 2D fractal surface with theoretical $FD_t = 2.7$ (i.e. a Hurst coefficient of 0.3) was first generated. The theoretical FD (FD_t) is the FD which the artificial surface was generated with (cf. Figure 4.8). The FD_t is considered as the target FD that a correctly-working algorithm should come to. Thus, in the end, FD_c, which is the calculated FD, must come as close as possible to FD_t. In Figure 4.9 it is visible that over most of the scales the rose plots look circular, which is an indication of the structure being isotropic, i.e. it changes the same regardless of the direction considered. It is also obvious that over scales 1-3 the calculated FD_c is approximately 2.7, close to the theoretical FD_t. Over scales 4-6 the surface doesn't seem as isotropic anymore, the value of 2.7 being detected only in certain directions, but there is still a tendency of circular plots. Over scales 7-9 the plots are not circular anymore and the FD_c varies too much from the expected FD_t. The reason why over larger scales this can happen may be that the algorithm generating the fractal surface makes use of a random number and therefore the generated structure depends on this random number. This number is responsible for how the structures of similar intensities are distributed across the entire image and this distribution may be detected by the VOT algorithm over bigger scales, since the bigger the scale, the more structure is caught up in one calculation.

The same behavior as described above can be seen when looking at Figure 4.10 (4.11 respectively) and Figure4.12 (4.13 respectively). The first Figure relates to a fractal

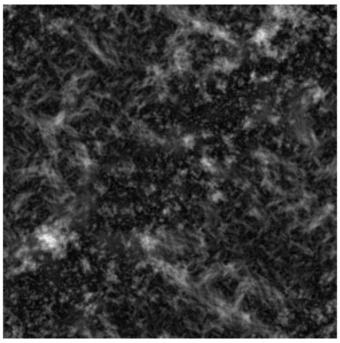

Figure 4.8: Generated isotropic 2D fractal surface with theoretical $FD_t = 2.7$.

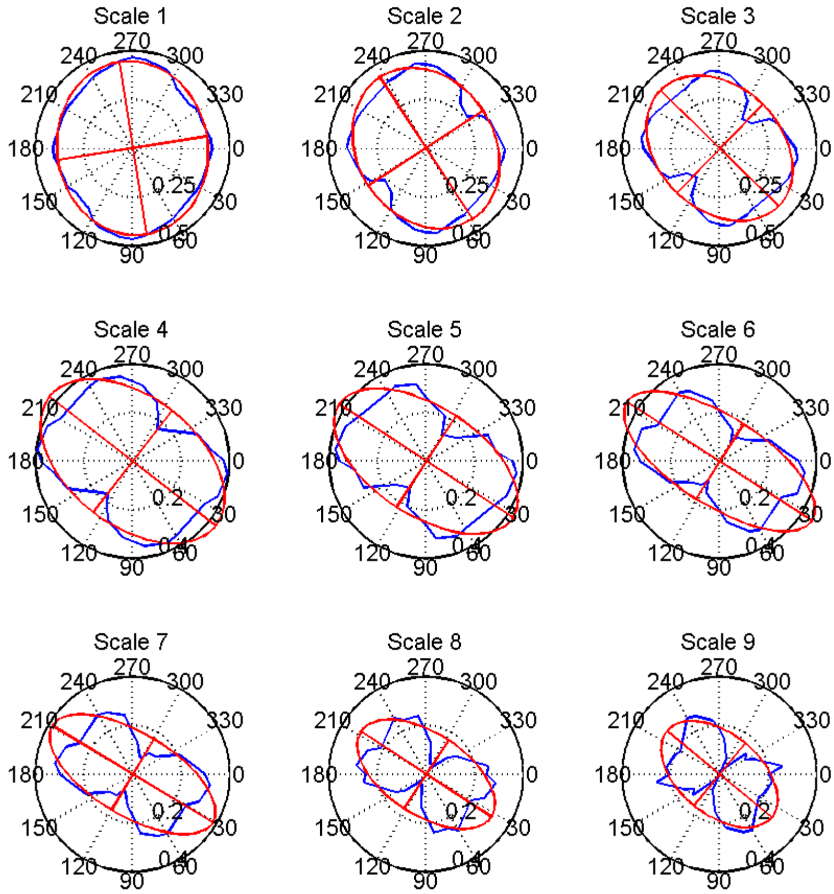

Figure 4.9: Rose plots of orientation (blue) of the Hurst coefficients for each scale and ellipses fitted (red) for surface from Figure 4.8.

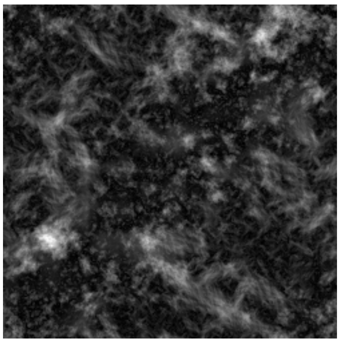

Figure 4.10: Generated isotropic 2D fractal surface with theoretical $FD_t = 2.5$.

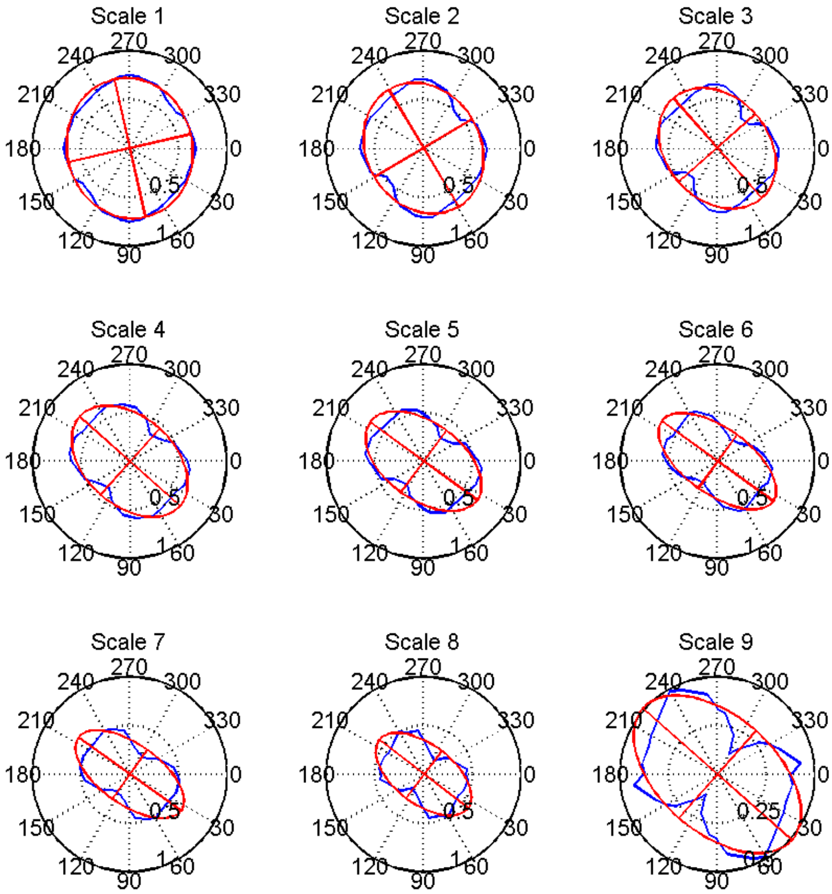

Figure 4.11: Rose plots of orientation (blue) of the Hurst coefficients for each scale and ellipses fitted (red) for surface from Figure 4.10.

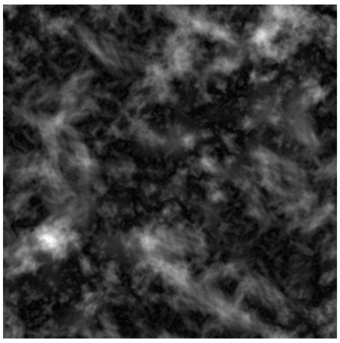

Figure 4.12: Generated isotropic 2D fractal surface with theoretical $FD_t = 2.3$.

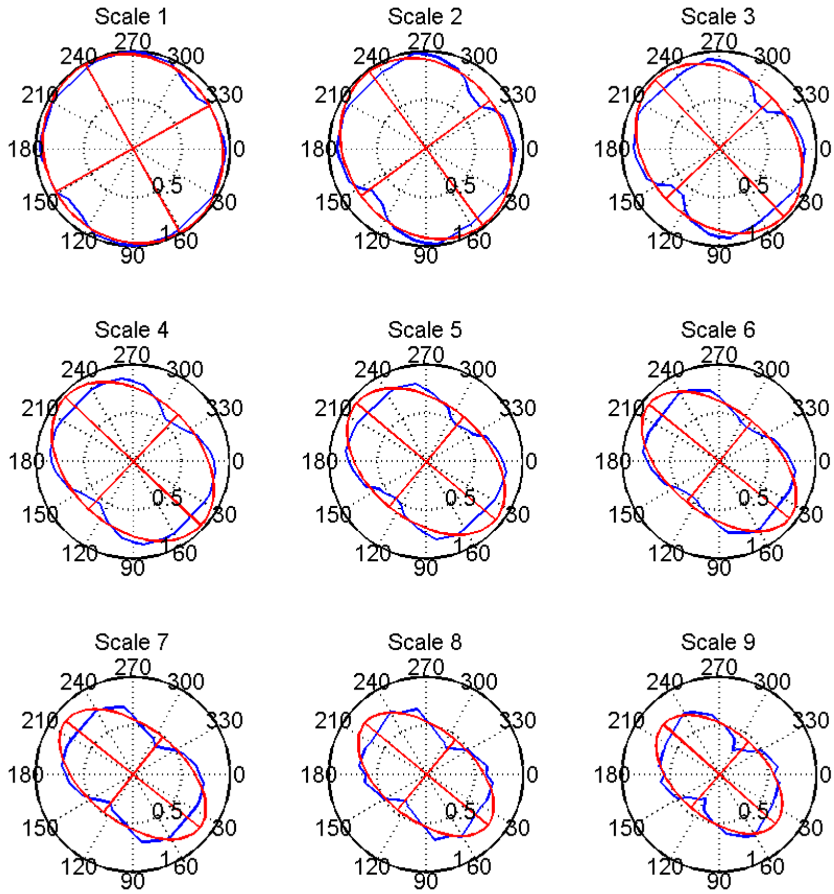

Figure 4.13: Rose plots of orientation (blue) of the Hurst coefficients for each scale and ellipses fitted (red) for surface from Figure 4.12.

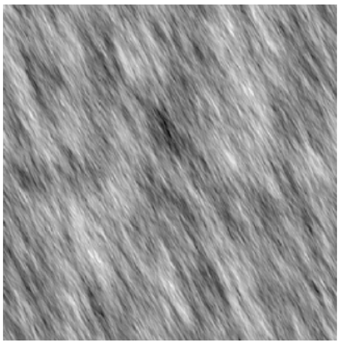

Figure 4.14: Generated anisotropic 2D fractal surface with theoretical $FD_t = 2.6$ in 30 degree direction and $FD_t = 2.2$ in 120 degree direction [WPS10, p. 2205].

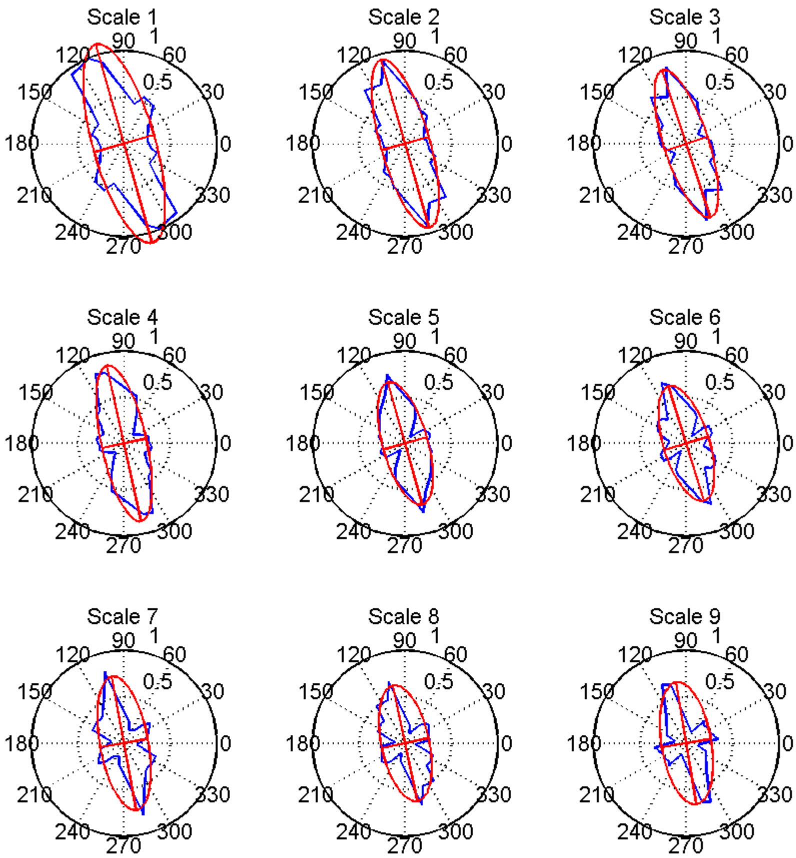

Figure 4.15: Rose plots of orientation (blue) of the Hurst coefficients for each scale and ellipses fitted (red) for surface from Figure 4.14.

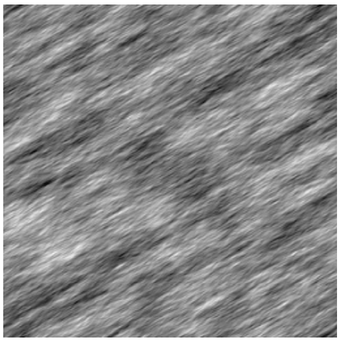

Figure 4.16: Generated anisotropic 2D fractal surface with theoretical $FD_t = 2.6$ in 120 degree direction and $FD_t = 2.2$ in 30 degree direction [WPS14, p. 7].

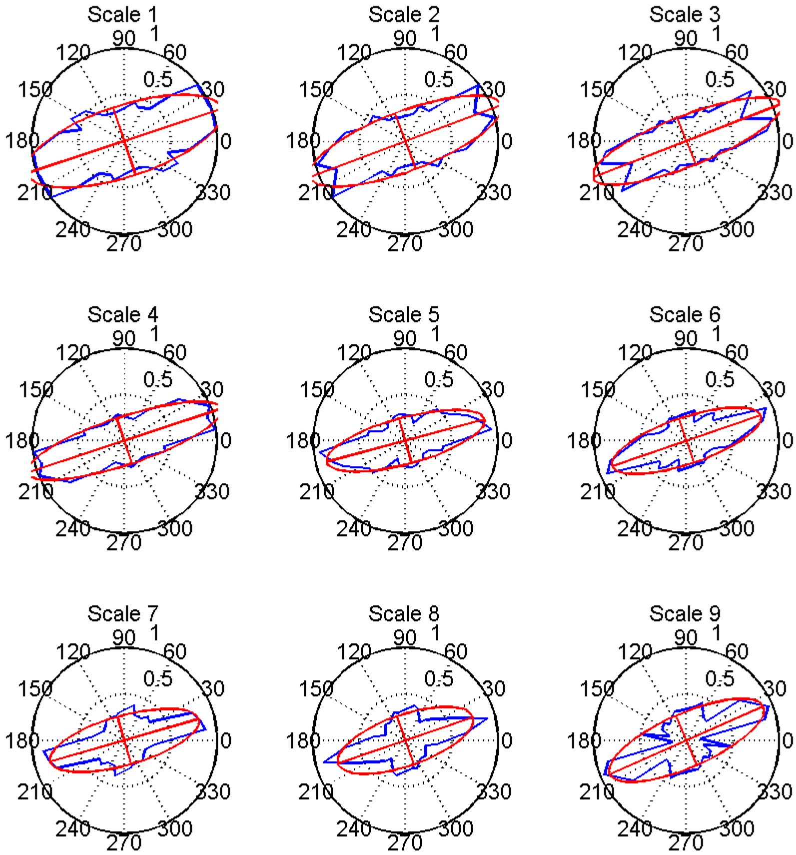

Figure 4.17: Rose plots of orientation (blue) of the Hurst coefficients for each scale and ellipses fitted (red) for surface from Figure 4.16.

surface with $FD_t = 2.5$, while the second relates to a generated fractal surface with $FD_t = 2.3$. As a possible conclusion, the small image sizes (i.e. scales 1-3) alone give a better insight into the complexity of the structure.

In the case of the anisotropic surfaces, an algorithm based on the inverse Fourier Transform can be used to generate 2D fractal surfaces with a known FD_t in a particular direction. However, we did not manage to have access to the algorithm in discussion and as a consequence we used reprinted versions of the images generated by Wolski [WPS14, p. 7], [WPS10, p. 2205].

First, in Figures 4.14 and 4.15 one can see an anisotropic fractal surface and the results returned by the VOT algorithm after analyzing it. The surface was generated with a given FD_t of 2.6 (or Hurst coefficient of 0.4) in direction 30° and a given FD_t of 2.2 (or Hurst coefficient of 0.8) in direction 120°. The values on the rose plots and the form of the plots suggest that this implementation of VOT is indeed sensitive to surface orientation, correctly detecting the tilt of the 'artificial trabeculae'. At the moment of writing this paper the degree of similarity between the artificially-generated surfaces and real trabecular surfaces is not known to us.

A second example can be seen in Figures 4.16 and 4.17. This surface has a completely other main orientation compared to the previous surface, featuring a FD_t of 2.6 in direction 120° and a FD_t of 2.2 in direction 30° (or Hurst coefficients of 0.4 and 0.8 respectively). The orientation and the theoretical FD_t-s seem to be detected correctly in this case as well.

In both cases there are obviously scales that overestimate or underestimate the FDs. This can happen because of the same reasons as with the isotropic surfaces: the higher the measurement scale, the more structure gets caught into calculations, the more affected are the results. The other way around also applies: the smaller the measurement scale, the less structure is considered into calculations, the less are the results affected by the structure.

4.6 Results

As mentioned earlier, the ultimate goal of an algorithm like VOT is differentiate OA-affected from non-affected TB in different stages of OA progression. Once that the algorithm was tested in Section 4.5, it can be applied to real bone surfaces of controls (patients without radiographic OA) and cases (patients with radiographic OA) with a hope of finding a significant difference between the two classes.

First, a ROI from the lateral part of the TB, extracted from a radiograph of a patient diagnosed with OA, was directly compared to a ROI extracted from a radiograph of a person with healthy knee TB. The results can be seen in Figures 4.18 and 4.19 for the osteoarthritic bone and in Figures 4.20 and 4.21 for the fine bone. At a first glance, the VOT is correctly detecting the orientation of the surface (i.e. of the trabeculae segments) in both cases. There is an important difference though, namely that in the case of the

OA bone, the main orientation seems to be distorted on the right side of the ROI (Figure 4.18), while in the case of the healthy bone, the main orientation is more pronounced. The disconnected trabeculae on the right side are a clear indication of OA. There is clearly no main orientation at high magnifications, thus the damage being mainly detected by the smaller scales (1-3). These tend to indicate isotropy, which is uncharacteristic for a healthy bone. Moreover, in the rose plots one can see that in the case of OA bone, the fitted ellipses show an alternating behavior, switching their deviation as the measurement scale grows, while in the case of the healthy bone, the deviations of the ellipses seem to be consistent over all nine scales. Another important aspect which can be derived from the plots is that in the case of OA bone, the S_{tb} parameter (the half of the length of the major axis), which is also directly related to the FD or FSs in the vertical direction, stays around the value of 0.25, while the same parameter in the case of the healthy bone goes above 0.5 over most of the scales. This observation also supports the statement made above, that the OA bone is damaged (i.e. the trabeculae are disconnected and there is no general orientation in the structure): the value of 0.25, which is lower than 0.5 (see Section 2.4) and is thus indicating a 'wild' or a rougher surface, which in other words means a distorted structure. Considering that S_{tb} is measured along the direction of the greatest smoothness, the S_{ta} (which describes the greatest roughness in the surface) is even smaller, indicating a possibly severely damaged TB.

The vertical and horizontal direction are of particular importance in the study of TB due to the compressive stress that permanently acts along the bone (vertical direction), determining expansion in the horizontal direction as well. The presence of forces inside the bone is normal, because otherwise the locomotion would not be possible, but if the bone is damaged or deformed in some way, these forces can act abnormally, affecting the orientation of trabeculae inside the TB.

Second, the algorithm was used on the radiograph from Figure 4.22, which belongs to a person with radiographic OA and valgus deformation (meaning that the foot is bent outwards and as a consequence the joint space narrowing is reduced in the lateral compartment of the TB). As a consequence, it is interesting to analyze both sides of the bone to see if the valgus deformation produces some changes in the corresponding TB compartment. The extracted ROI and its VOT report from the lateral compartment can be seen in Figures 4.23 and 4.24, while the ones from the medial compartment are illustrated in Figures 4.25 and 4.26. Again, as in the first example, the orientations are correctly detected in both compartments, but the trabeculae within the lateral part are damaged because of to the pressure of bone-on-bone contact due to narrowing of joint space. This statement can be supported by scales 7-9 which show more than one dominant direction in the structure, whereas scales 1-6 show only one. This can also be observed with the naked eye. In the lateral compartment there is no much structure left and many holes can be seen, whereas in the medial compartment the trabeculae compartments are visible. From the Hurst coefficients' point of view, the same applies as in the first example: lower values for the damaged compartments and higher for the healthy ones.

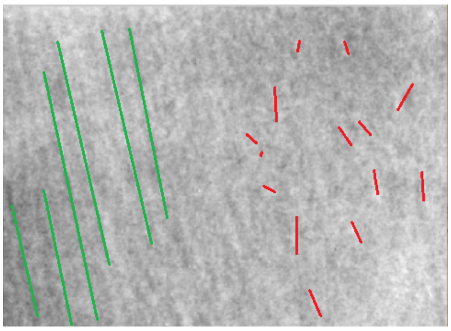

Figure 4.18: OA bone surface. Disconnected (red) and continous trabeculae (green).

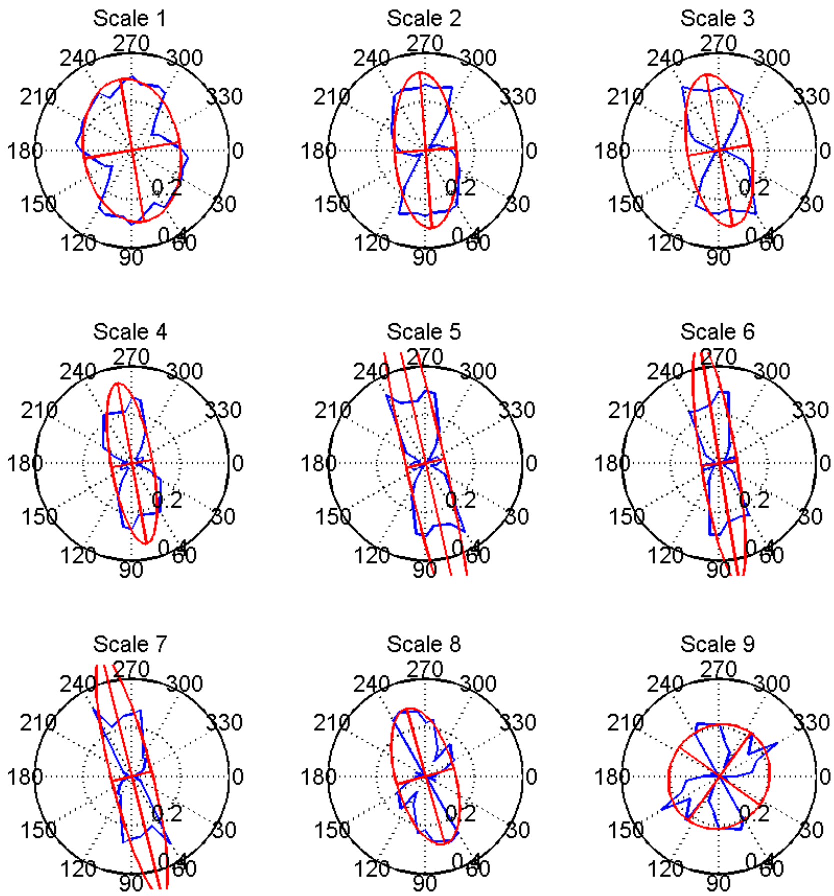

Figure 4.19: VOT report on image from Figure 4.18.

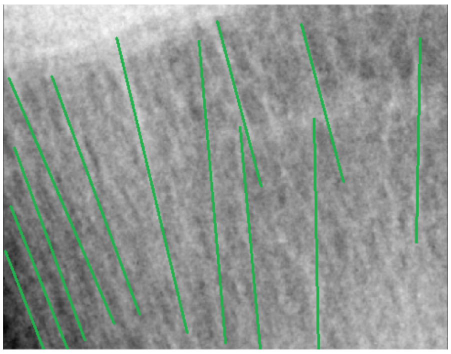

Figure 4.20: Healthy bone surface with countinous trabeculae (green)

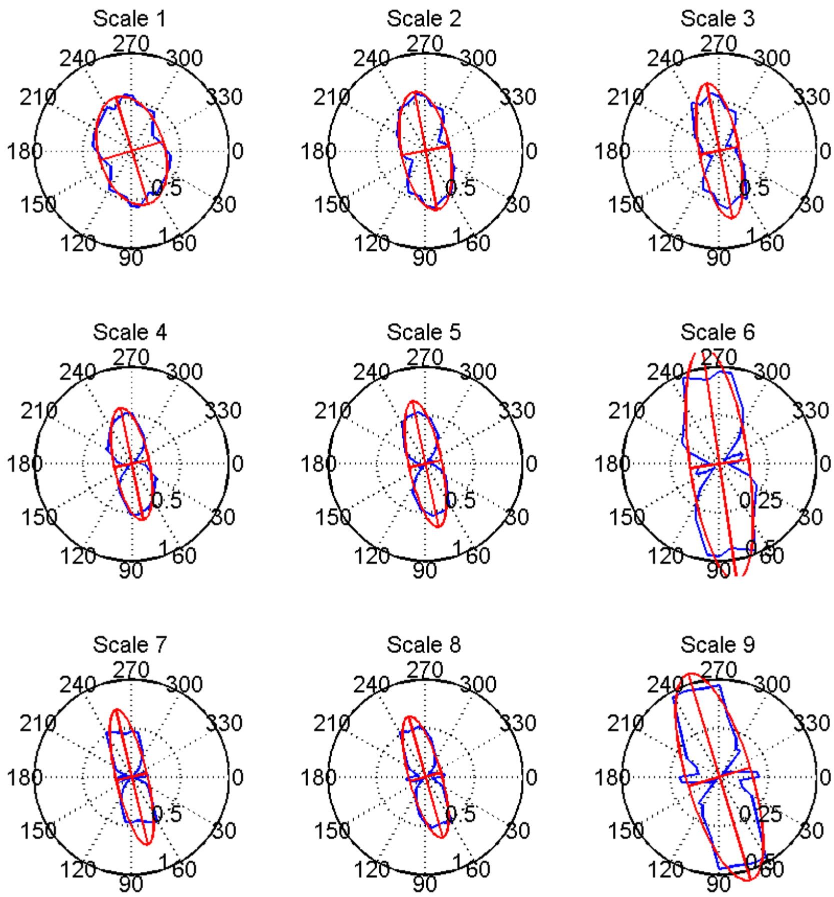

Figure 4.21: VOT report on image from Figure 4.20.

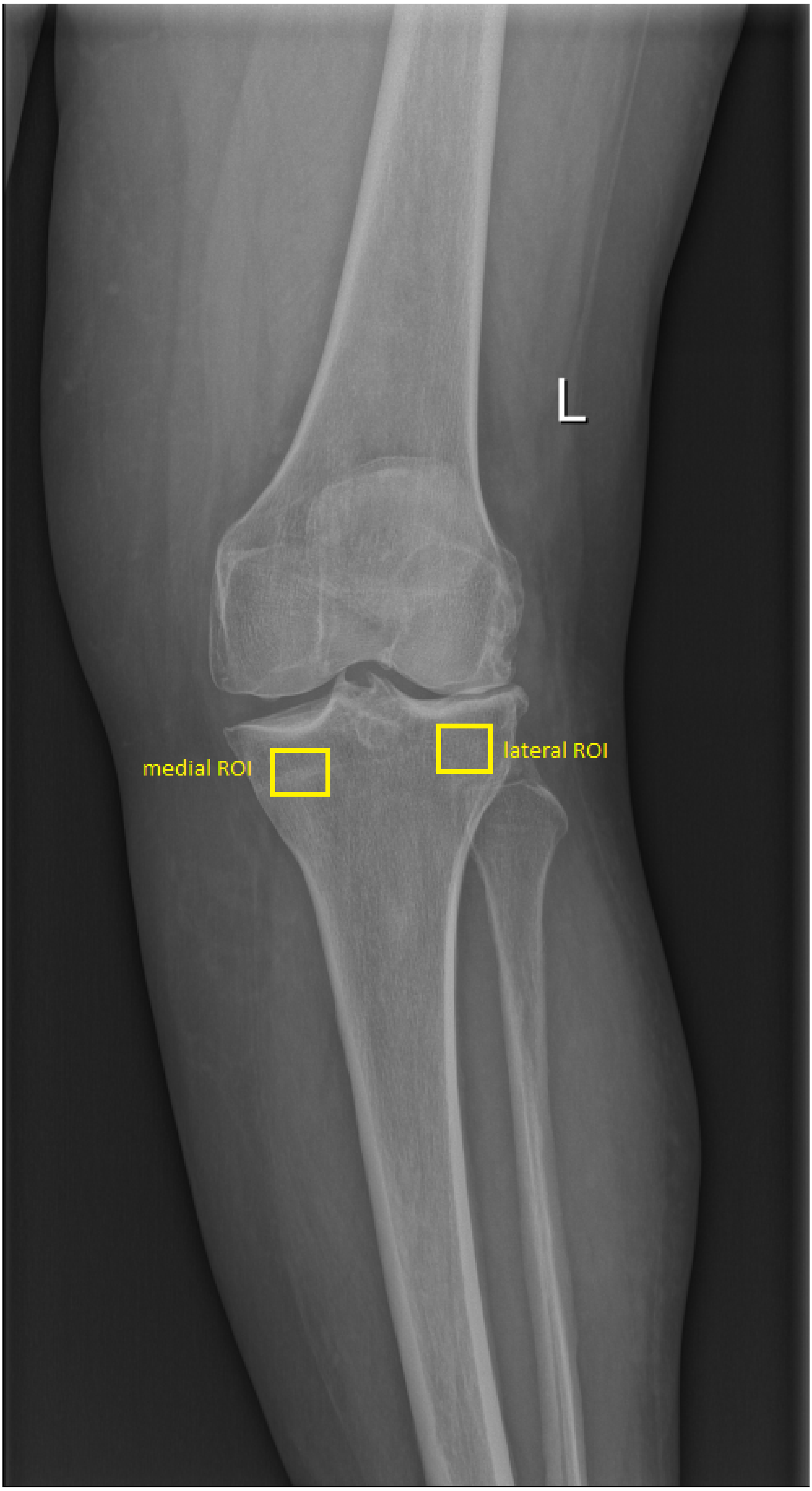

Figure 4.22: Bone with valgus deformation and radiographic OA. Medial and lateral compartments are marked in yellow.

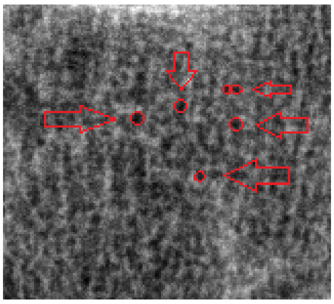

Figure 4.23: ROI from lateral compartment extracted from 4.22. The holes that indicate a poor, damaged structure are marked in red.

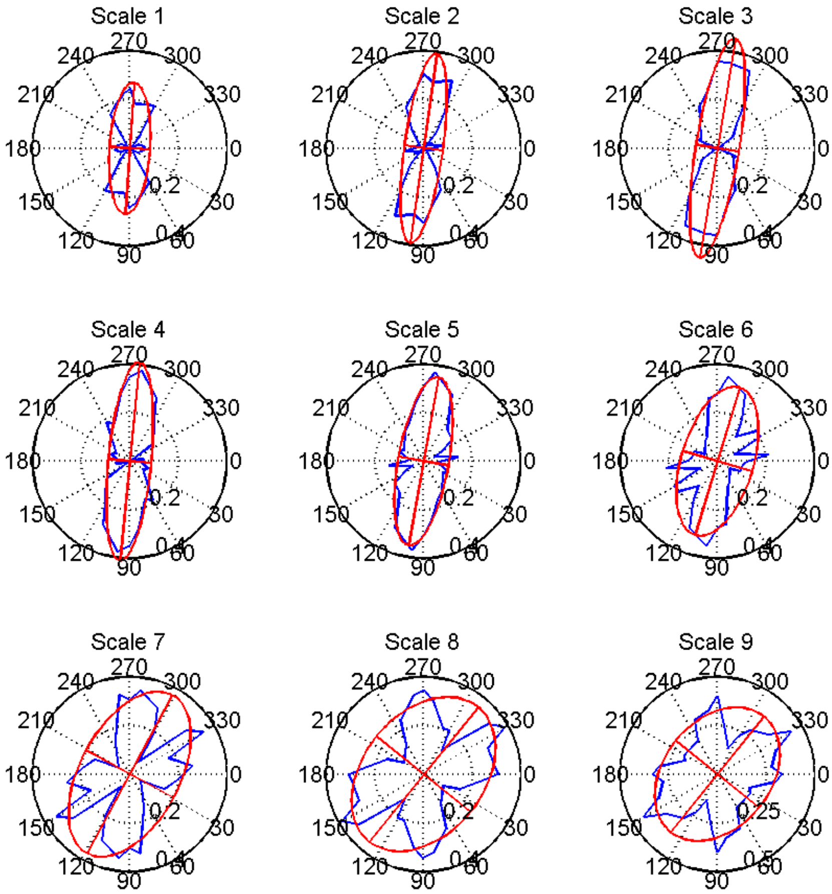

Figure 4.24: VOT report on image from Figure 4.23

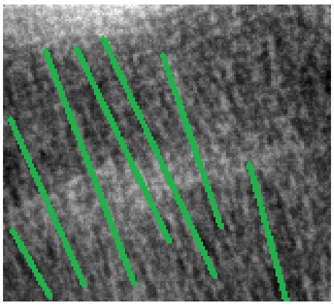

Figure 4.25: ROI from medial compartment extracted from 4.22. The continous trabeculae are marked (green).

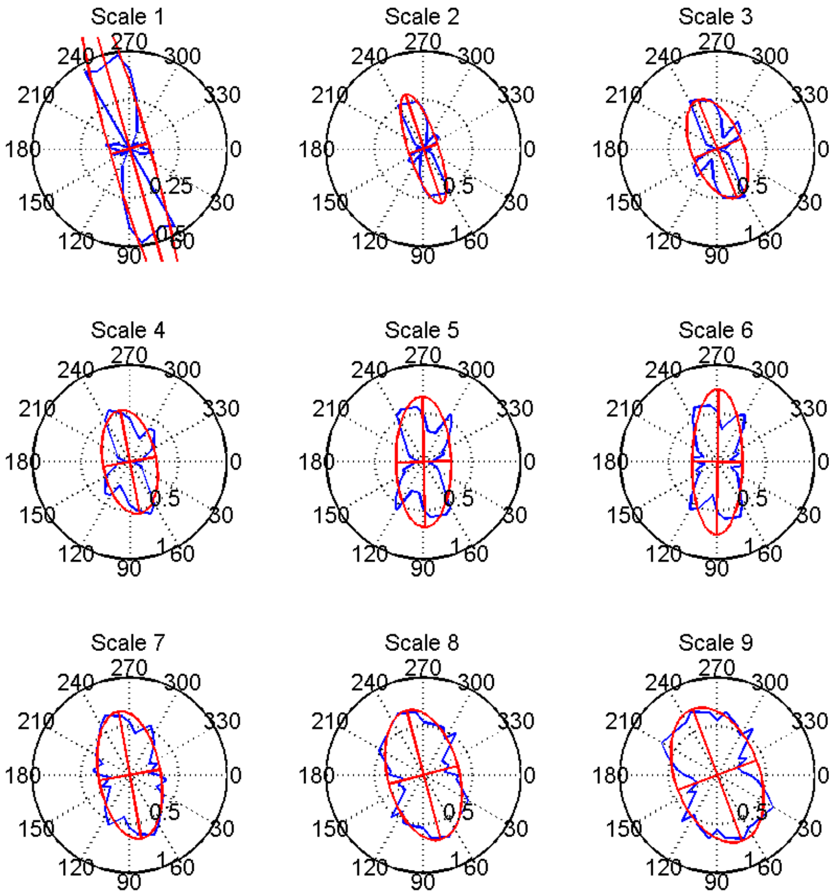

Figure 4.26: VOT report on image from Figure 4.25

CHAPTER 5

Conclusion and Future Work

The images presented in Section 4.6 as examples for testing the VOT method on real TB were carefully selected so their features are visible to the eye, as well as 'numerically' detectable by the algorithm. However, OA and non-OA TB may indicate small differences as well. In this case, the algorithm, in its original form, performs not as good as expected.

A series of system-dependant factors such as different types of noise, contrast shift, blur, exposure (different mAs values), pixel resolution and projection angle can influence the results of the VOT algorithm. Therefore, these influences must be investigated in future works. Aside from system-dependent factors there are human-dependent factors which must be taken into account when testing the accuracy of VOT. For example, as shown in Chapter 3, there can be different grades of OA after the KL scoring system. Thus, different grades of JSW (joint space width), sclerosis, bone deformity and osteophytes can have different impacts on the FD of the bone surface. It is very hard to find enough patients of the same age, gender and same bone affections to build a reliable statistical model and to know if VOT is indeed accurate or not. Once the relation of all the mentioned factors to the FD of the surface is discovered, the calibration of VOT algorithm becomes possible, making it able to correctly analyze all kinds of surfaces, regardless of conditions.

The VOT method has been recently proven to not be able to characterize very small texture regions due to its limitations that stem from the fact that the search region is of fixed size and features. As an improvement Wolski developed a flexible version of VOT called AVOT (augmented-VOT)[WPS14, p. 5]. In our next studies we will investigate this method and possible improvements to it as well.

This work has presented a way of analyzing and describing the complex structure of the trabecular bone using the VOT method. There exist a lot of ways of analyzing different types of fractals, of different forms, complexities and in different fields VOT being just one approach applicable to fractals in medical image analysis. This gives an idea of how complicated to describe fractal surfaces can be. In the future there the approaches may also be differentiated after each tissue type. In 2006 during the Nobel Prize Ceremony, Mandelbrot held his 24/7 Lecture on fractals calling them: 'beautiful, damn hard, increasingly useful. That's fractals!'.

List of Figures

List of Tables

Bibliography

[BW04] Christopher Buckland-Wright. Subchondral bone changes in hand and knee osteoarthritis detected by radiography. *Osteoarthritis and Cartilage*, 12(SUPLL.):10–19, 2004.

[Cla86] Keith C. Clarke. Computation of the fractal dimension of topographic surfaces using the triangular prism surface area method. *Computers and Geosciences*, 12(5):713–722, 1986.

[Fal04] K Falconer. *Fractal Geometry: Mathematical Foundations and Applications*. Wiley, 2004.

[FP96] N. L. Fazzalari and Ian H. Parkinson. Fractal Dimension and Architecture of Trabecular Bone. *Journal of Pathology*, 178(1):100–105, 1996.

[Ger98] W G Geraets. Comparison of two methods for measuring orientation. *Bone*, 23(4):383–388, 1998.

[GMH+14] Catherine M Gdyczynski, Amir Manbachi, SayedMasoud Hashemi, Bahman Lashkari, and Richard S C Cobbold. On estimating the directionality distribution in pedicle trabecular bone from micro-CT images. *Physiological Measurement*, 35(12):2415, 2014.

[GS01] Tilmann Gneiting and Martin Schlather. Stochastic models which separate fractal dimension and Hurst effect. *SIAM Review*, 46(2):269–282, 2001.

[HBS65] H. E. Hurst, R. P. Black, and Y. M. Simaika. Long-term Storage: An Experimental Study. 1965.

[HSD73] Robert Haralick, K. Shanmugan, and I. Dinstein. Textural features for image classification, 1973.

[Hur51] H. E. Hurst. Long Term Storage Capacity of Reservoirs. *Transactions of the American Society of Civil Engineers.*, (116):770–799, 1951.

[KL57] J. H. Kellgren and J. S. Lawrence. Radiological Assessment of Osteo-Arthrosis. *Annals of the rheumatic diseases*, 16(4):494–502, 1957.

[KMNY01] Tony M. Keaveny, Elise F. Morgan, Glen L. Niebur, and Oscar C. Yeh. Iomechanics of. *Annual Review of Biomedical Engineering*, (3):307–333, 2001.

[KWCZ] L Kamibayashi, U P Wyss, T D V Cooke, and B Zee. Changes in mean trabecular orientation in the medial condyle of the proximal tibia in osteoarthritis. *Calcified Tissue International*, 57(1):69–73.

[KWCZ95] L Kamibayashi, U P Wyss, T D V Cooke, and B Zee. Trabecular microstructure in the medial condyle of the proximal tibia of patients with knee osteoarthritis. *Bone*, 17(1):27–35, 1995.

[LB09] R. Lopes and N. Betrouni. Fractal and multifractal analysis: A review. *Medical Image Analysis*, 13(4):634–649, 2009.

[LCW+14] Yu Liu, Lingyu Chen, Heming Wang, Lanlan Jiang, Yi Zhang, Jiafei Zhao, Dayong Wang, Yuechao Zhao, and Yongchen Song. An improved differential box-counting method to estimate fractal dimensions of gray-level images. *Journal of Visual Communication and Image Representation*, 25(5):1102–1111, 2014.

[LDS09] Jian Li, Qian Du, and Caixin Sun. An improved box-counting method for image fractal dimension estimation. *Pattern Recognition*, 42(11):2460–2469, 2009.

[Man83] B B Mandelbrot. *The Fractal Geometry of Nature*. Einaudi paperbacks. Henry Holt and Company, 1983.

[MH05] B B Mandelbrot and R L Hudson. *Misbehavior of Markets*. Basic Books, 2005.

[MKA+98] S. Majumdar, M. Kothari, P. Augat, D. C. Newitt, T. M. Link, J. C. Lin, T. Lang, Y. Lu, and H. K. Genant. High-resolution magnetic resonance imaging: Three-dimensional trabecular bone architecture and biomechanical properties. *Bone*, 22:445–454, 1998.

[MWC68] B B Mandelbrot, J R Wallis, and Thomas J Watson I B M Research Center. *Noah, Joseph Son of Jacob, and Operational Hydrology*. IBM Thomas J. Watson Research Center, 1968.

[MWTBW05] Elizabeth A. Messent, Rupert J. Ward, Carol J. Tonkin, and Christopher Buckland-Wright. Tibial cancellous bone changes in patients with knee osteoarthritis. A short-term longitudinal study using Fractal Signature Analysis. *Osteoarthritis and cartilage / OARS, Osteoarthritis Research Society*, 13(6):463–70, 2005.

[PF00] Ian H. Parkinson and N. L. Fazzalari. Methodological principles for fractal analysis of trabecular bone. *Journal of Microscopy*, 198(2):134–142, 2000.

[PFS+12] H O Peitgen, Y Fisher, D Saupe, M McGuire, R F Voss, M F Barnsley, R L Devaney, and B B Mandelbrot. *The Science of Fractal Images.* Springer New York, 2012.

[PLDS08] P. Podsiadlo, L. S. Lohmander, L. L. Dahl, and G. W. Stachowiak. Osteoarthritis and Cartilage Vol . 14 , Supplement B S137 TRABECULAR BONE TEXTURE CHANGES IN OSTEOARTHRITIC KNEES DETECTED BY PLAIN RADIOGRAPHY AND FRACTAL METHODS. *Osteoarthritis and Cartilage*, 14:Supplement B S137, 2008.

[PSB88] H O Peitgen, D Saupe, and M F Barnsley. *The Science of fractal images.* Springer-Verlag, 1988.

[PSD+10] P. Podsiadlo, G. W. Stachowiak, L. Dahl, L. S. Lohmander, and M. Englund. Differences in trabecular bone texture between knees with and without radiographic osteoarthritis detected by directional fractal signature method. *Osteoarthritis and Cartilage*, 18(5):323–329, 2010.

[SFQ97] A. De Santis, M. Fedi, and T. Quarta. A revisitation of the triangular prism surface area method for estimating the fractal dimension of fractal surfaces. *Annals of Geophysics*, 40(4), 1997.

[SH00] Chen Shuyue and Lu Hongnian. Noise Characteristic and its Removal in Digital Radiographic System. In *ROMA 2000, WCNDT, World Conference on Non-Destructive Testing, 15*, page 8, Rome, 2000.

[V12] Bino Sebastian V. Grey Level Co-Occurrence Matrices: Generalisation and Some New Features. *International Journal of Computer Science, Engineering and Information Technology*, 2(2):151–157, 2012.

[Wol67] Marcin Wolski. How long is the coast of Britain? Statistical self-similarity and fractional dimension. *Science*, (156):636–638, 1967.

[WPS09] M Wolski, P Podsiadlo, and G W Stachowiak. Directional fractal signature analysis of trabecular bone: evaluation of different methods to detect early osteoarthritis in knee radiographs. *Proceedings of the Institution of Mechanical Engineers. Part H, Journal of engineering in medicine*, 223(2):211–236, 2009.

[WPS10] M. Wolski, P. Podsiadlo, and G. W. Stachowiak. Applications of the variance orientation transform method to the multiscale characterization of surface roughness and anisotropy. *Tribology International*, 43(11):2203–2215, 2010.

[WPS14] M. Wolski, P. Podsiadlo, and G. W. Stachowiak. Directional fractal signature methods for trabecular bone texture in hand radiographs: Data from the Osteoarthritis Initiative. *Medical Physics*, 41(8):081914, 2014.